Structural and Multidisciplinary Optimization (2021) 64:3911–3935
https://doi.org/10.1007/s00158-021-03068-x

RESEARCH PAPER

Homogenization in a simpler way: analysis and optimization of periodic unit cells with Cauchy–Born hypothesis

Kun Wang[1] · Ming Cai[1] · Pingzhang Zhou[1] · Gengkai Hu[1]

Received: 10 May 2021 / Revised: 19 July 2021 / Accepted: 24 August 2021 / Published online: 28 September 2021

Abstract
Asymptotic expansion based homogenization has been widely used to predict the effective macroscopic properties of periodic unit cells (PUCs). In this work, we show that the homogenization process can be done in a much more elegant manner for both continuum and discrete PUCs by taking advantage of the Cauchy–Born's hypothesis, which is a widely used rule in the area of solid physics to relate the position of the atoms in a crystal lattice and the overall strain of the medium. It is shown that in the proposed method, the derivation process of the effective elasticity tensor is quite easy and can rely entirely on commercial CAE software (e.g., ANSYS, ABAQUS, etc.) to accomplish the homogenization task. In detail, after the discretization of the unit cell with finite elements, one only needs to apply *affine boundary conditions* at the exterior boundaries of the unit cell and then call the FEA solver to find the static displacement field under such affine boundary conditions. The entries of the elasticity tensor can then be expressed using the stain energy of the unit cell. After deriving the sensitivity information of the Cauchy–Born hypothesis based homogenization process, the inverse homogenization process, which attempts to find the optimal layout exhibiting pre-determined desirable material properties, can be implemented in a straightforward way as well. Some numerical examples are tested and compared with the results in the literature. It is showed that the results of both the homogenization and inverse homogenization examples obtained by our method agree very well with the ones in the literature, demonstrating the validity of the Cauchy–Born hypothesis based numerical homogenization method.

Keywords Cauchy–Born hypothesis · Numerical homogenization · Inverse homogenization · Topology optimization

1 Introduction

Composites have found extensive applications in all kinds of engineering branches since they have superior mechanical, thermal, or electromagnetic properties that cannot be achieved by any of the constituent materials acting alone (Gibson 2016). Directly calculating the response of a macroscopic engineering structure composed of micro-heterogeneous materials, incorporating all of the micro-scale features is beyond the ability of even the fastest computer at this time. The homogenization theory, which is used to find the effective homogeneous properties of composites so that the micro-scale heterogeneities can be neglected if only the macro-scale response is of interest, is therefore extremely advantageous since the computation burden can be reduced to a great extent. On the other hand, the homogenization theory also makes it possible to predict the properties of a composite material even before it is engineered (Bakhvalov and Panasenko 1984) and consequently to virtually design a composite with predetermined or extremum properties (Sigmund 1994b; Andreassen et al. 2014) by *manipulating* its microstructure. In the literature, this procedure is usually termed as the inverse homogenization process (Sigmund 1994b).

Generally there are two kinds of composites (Zohdi and Wriggers 2008), the one composed of randomly distributed constituents and the one composed of periodically tessellated constituents. The former is called as a random medium while the latter is called as a periodic medium. We emphasize that these two concepts are not the same although they have close relationships. The basis element of the random medium is called as the representative

Responsible Editor: Seonho Cho

✉ Pingzhang Zhou
zhoupz2021@bit.edu.cn

[1] School of Aerospace Engineering, Beijing Institute of Technology, Beijing, People's Republic of China

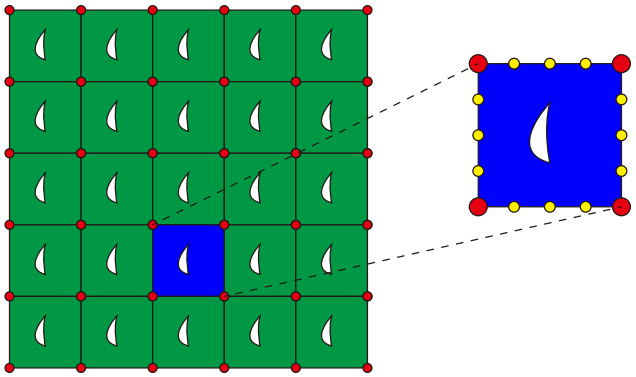

Fig. 1 Periodic unit cells. The left side shows the periodic media composed of tessellations of unit cells, the right shows one basis of the unit cell. Red dots denote the corner nodes defining the lattice, yellow dots denote the boundary nodes other than the corner nodes. (Color figure online)

volume element (RVE) while that of the periodic medium is called as the periodic unit cell (PUC). In this paper we concentrate on the periodic medium, i.e., the composites with PUCs (see Fig. 1). The periodicity feature implies that under macroscopic loads all physical quantities (e.g. displacement, strain, stress, etc.) should have the same period with the geometry. Therefore, it is possible to take advantage of mathematical tools to calculate quantitatively the exact values of the effective characteristics. Take mechanic properties as an example, exact values of the effective elasticity tensor can be obtained for periodic media; but for random media, only upper and lower bounds can be available for relatively simple microstructures (e.g., isotropic continuum or transversely isotropic continuum).

Asymptotic expansion based homogenization (AH) (Hassani and Hinton 1998a, b; Kalamkarov and Georgiades 2004) is a powerful and well-known tool to calculate the effective elastic moduli of PUCs. Its basic idea is to take the asymptotic expansion of the solution in terms of a small parameter ϵ, which is the ratio of the period of the unit cell to the characteristic length of the whole structure. By substitution the asymptotic expansion of the solution into the state equation, a series of homogenized equations can be obtained, from which the effective coefficients describing the macroscopic properties of the medium can then be derived. Since AH can guarantee the periodicity of both the displacement and traction (Xia et al. 2003), it can find accurate effective moduli when compared with the commonly used method of RVE in the community of composite mechanics. In the RVE method, however, it is generally acknowledged that the homogeneous displacement or traction boundary condition cannot ensure the periodicity of displacement and traction at the same time (Xia et al. 2003). Due to its accuracy, the AH has been widely used to predict the effective moduli of periodic unit cells (Hassani and Hinton 1998a) and to design microstructures with predetermined mechanic (Sigmund 1994b, 1995; Andreassen et al. 2014) or thermal properties (Sigmund and Torquato 1996).

The AH has a solid mathematical foundation, but the derivation and implementation process is cumbersome. To derive the effective parameters, one needs to obtain a set of characteristic functions which are periodic solutions under a set of uniform initial strain exerted on the unit cell. In practice, the above uniform initial strain is equivalently converted to nodal forces with the assistance of virtual work principle. The nodal force takes the form of $\boldsymbol{F} = \int_Y \boldsymbol{B}^\top \boldsymbol{D}\, \mathrm{d}\boldsymbol{y}$, thus the strain–displacement matrix $\boldsymbol{B}$, which is usually not available from commercial FEA software (e.g. ABAQUS, ANSYS, COMSOL, etc.), plays a key role in the numerical implementation of the AH method. This fact makes it not easy to implement the AH based on the functionalities of commercial FEA software. Some open-source codes are available in the literature (Andreassen and Andreasen 2014; Dong et al. 2019; Christoff et al. 2020), this may help ease the difficulty of using the AH method, but such codes cannot make full use of the geometry modelling, meshing and efficient solving capabilities of commercial FEA software. This problem can be circumvented by converting the uniform strain into corresponding nodal displacement vector (Cheng et al. 2013). Another possible remedy is to apply the uniform strain field by means of pre-strain caused by heat source (Yuan and Fish 2008), but this would in turn transform the original problem into a thermal–mechanic coupling problem and increase the computational complexity. In summary, all these techniques are tricky and not straightforward.

Periodic media formed by tessellating unit cells, which are composed of corner nodes and linking elements (rods, beams, or continuum body), behave similar to the crystals. Nodes are analogous to atoms and linking elements are analogous to chemical bonds. The Cauchy–Born hypothesis, a widely used rule in the area of solid physics, relates the position of the atoms in a crystal lattice and the overall strain of the medium. By using the Cauchy–Born hypothesis (Ericksen 2008), there is no need to resort to the double-scale expansion in order to set up the transitional relationship between macroscopic scale and microscopic scale, making the homogenization process extremely easy to understand and implement. Therefore, there have been some researches (Hutchinson and Fleck 2006; Vigliotti and Pasini 2012a, b; Gasparetto and ElSayed 2021) attempting to find the effective elastic moduli of truss-like or beam-like periodic discrete structures. Using Cauchy–Born periodic condition and matrix analyzing method, Hutchinson and Fleck (2006) calculated the effective elasticity tensor of two pin-jointed lattices, which can further correctly reflect the zero-energy deformation modes of the lattices. Vigliotti and Pasini (2012a, b) applied the Cauchy–Born periodic condition to periodic rigid-jointed frames. These works show that the

Cauchy–Born periodic condition is very suitable to carry out the homogenization of truss-like or beam-like periodic discrete structures.

In this article, we formally establish a uniform framework to calculate the effective elastic moduli of periodic media composed of either continuum or discrete constituents, or even combination of them. It will be shown that the whole homogenization process based on the Cauchy–Born hypothesis are easy and straightforward to understand. In the proposed method, one only needs to apply the Cauchy–Born periodic condition on the exterior boundary nodes and request the output of strain energy. The effective elastic moduli can then be expressed using the strain energy of the unit cell. It follows that the implementation of the proposed method can totally rely on commercial FEA software in a simple manner. The sensitivity analysis shows that the inverse homogenization process can also rely entirely on commercial FEA software, making the proposed method suitable for both the analysis and optimization of microstructures.

The remaining parts of this paper are arranged as follows. Section 2 gives a brief review on the asymptotic expansion based homogenization and its numerical implementation procedure. Section 3 elaborates the work flow of the Cauchy–Born hypothesis based numerical homogenization. Distinctions with the RVE method and the sensitivity analysis are also covered in this section. Sections 4 and 5 demonstrates the effectiveness of the proposed method in the analysis and optimization of all kinds of microstructures, respectively. Section 6 gives some discussions on the scale-invariance of the proposed CBNH method. Section 7 concludes this paper.

2 A brief introduction on asymptotic expansion based homogenization

Rigorous mathematical derivation of AH is both tricky and lengthy, so it is not practical to cover all the details on AH. Instead, we outline some key steps here. Readers are recommended to relevant references (Bakhvalov and Panasenko 1984; Hassani and Hinton 1998a, b; Kalamkarov and Georgiades 2004; Bensoussan et al. 1978) for more details.

2.1 Derivation of the effective elastic moduli

The basic hypothesis of AH is that the continuum is the periodic repetition of unit cells. The relation between macroscopic scale and microscopic scale can thus be given by $\boldsymbol{y} = \boldsymbol{x}/\epsilon$, where ϵ is a small number. Asymptotic expansion of the displacement u_i can be given by

$$u_i^\epsilon = u_i^{(0)}(\boldsymbol{x}) + \epsilon u_i^{(1)}(\boldsymbol{x},\boldsymbol{y}) + \epsilon^2 u_i^{(2)}(\boldsymbol{x},\boldsymbol{y}) + \cdots \tag{1}$$

Notice that in (1) it is assumed that the zero-order approximation term $u_i^{(0)}$ depends only on the macroscopic scale since it represents the average of macroscopic displacement. This assumption can indeed be proved true mathematically (Hassani and Hinton 1999), but are omitted here for simplicity. We use the superscript ϵ to emphasize that a variable is related to both the macroscopic and microscopic scale. The infinitesimal strain tensor is the symmetric gradient of the displacement, i.e.,

$$\varepsilon_{ij}^\epsilon(\boldsymbol{x}) = \epsilon^0 \varepsilon_{ij}^{(0)}(\boldsymbol{x},\boldsymbol{y}) + \epsilon^1 \varepsilon_{ij}^{(1)}(\boldsymbol{x},\boldsymbol{y}) + \cdots \tag{2}$$

The elasticity tensor is homogeneous in macroscopic scale but heterogeneous in the microscopic scale, i.e., $D_{ijkl}^\epsilon = D_{ijkl}(\boldsymbol{y})$. By using the Hooke's theorem, the stress tensor can be given by

$$\begin{aligned}\sigma_{ij}^\epsilon(\boldsymbol{x}) &= D_{ijkl}^\epsilon \varepsilon_{kl}^\epsilon \\ &= \epsilon^0 \sigma_{ij}^{(0)}(\boldsymbol{x},\boldsymbol{y}) + \epsilon^1 \sigma_{ij}^{(1)}(\boldsymbol{x},\boldsymbol{y}) + \cdots\end{aligned} \tag{3}$$

The equilibrium equation of the continuum reads as

$$\sigma_{ij,j}^\epsilon + f_i = 0, \text{ in } \Omega. \tag{4}$$

Substitute (3) into (4) and keep in mind that the equation should be satisfied for arbitrary small values of ϵ, we have the state equation of the AH method,

$$\frac{\partial}{\partial y_j} D_{ijkl}^\epsilon \left(\frac{\partial u_k^{(0)}}{\partial x_l} + \frac{\partial u_k^{(1)}}{\partial y_l} \right) = 0. \tag{5}$$

Now we introduce a *characteristic function* to relate the macroscopic displacement with the first order microscopic displacement,

$$u_k^{(1)} = -\phi(\boldsymbol{y})_k^{pq} \frac{\partial u_p^{(0)}}{\partial x_q}. \tag{6}$$

Substitute (6) into (5), we have the *equilibrium equation for the characteristic function*,

$$\frac{\partial}{\partial y_j} D_{ijpq}^\epsilon \left(\delta_{kp}\delta_{lq} - \frac{\partial \phi_p^{kl}}{\partial y_q} \right) = 0. \tag{7}$$

Substitute (6) into the expression of $\sigma_{ij}^{(0)}$ and integrate over the unit cell, we have

$$\overline{\sigma}_{ij}^{(0)} = D_{ijkl}^\heartsuit \frac{\partial u_k^{(0)}}{\partial x_l}, \tag{8}$$

where the *average macroscopic stress* is defined as

$$\overline{\sigma}_{ij}^{(0)} = \frac{1}{|\boldsymbol{Y}|}\int_Y \sigma_{ij}^{(0)}(\boldsymbol{x},\boldsymbol{y})\,\mathrm{d}\boldsymbol{y}, \tag{9}$$

the *equivalent elasticity tensor* is defined as

$$D_{ijkl}^{\heartsuit} = \frac{1}{|\boldsymbol{Y}|}\int_Y D_{ijpq}^{\epsilon}\left(\varepsilon_{pq}^{0(kl)} - \varepsilon_{pq}^{\phi(kl)}\right)\mathrm{d}\boldsymbol{y}, \tag{10}$$

and $\varepsilon_{pq}^{0(kl)}$, $\varepsilon_{pq}^{\phi(kl)}$ are given by

$$\varepsilon_{pq}^{0(kl)} = \frac{1}{2}\left(\delta_{kp}\delta_{lq} + \delta_{kq}\delta_{lp}\right), \tag{11a}$$

$$\varepsilon_{pq}^{\phi(kl)} = \frac{1}{2}\left(\frac{\partial \phi_p^{kl}}{\partial y_q} + \frac{\partial \phi_q^{kl}}{\partial y_p}\right). \tag{11b}$$

In (9) and (10), $\boldsymbol{Y} = [Y_1, Y_2, Y_3]^{\top}$ in three-dimensional case denotes the period vector of the unit cell, $|\boldsymbol{Y}|$ is thus the volume of the unit cell in three-dimensional case and the area in two-dimensional case.

2.2 Finite element solution of the equivalent elasticity tensor

The weak form of the equilibrium equation (7) can be stated as follows.

$$\forall \boldsymbol{v} \in \boldsymbol{\Phi} \quad \text{, find } \boldsymbol{\phi}_p^{kl} \in \boldsymbol{\Phi}, \text{ such that}$$
$$\int_Y \varepsilon_{ij}^{v} D_{ijpq}^{\epsilon} \varepsilon_{pq}^{\phi(kl)}\,\mathrm{d}\boldsymbol{y} = \int_Y \varepsilon_{ij}^{v} D_{ijpq}^{\epsilon} \varepsilon_{pq}^{0(kl)}\,\mathrm{d}\boldsymbol{y}, \tag{12}$$

where the admissible functional space $\boldsymbol{\Phi}$ is given by

$$\boldsymbol{\Phi} = \left\{\boldsymbol{u} | u_i \in H^1(Y); u_i(\boldsymbol{r} + n\boldsymbol{Y}) \equiv u_i(\boldsymbol{r})\right\}. \tag{13}$$

$H^1(Y)$ denotes the Sobolev space, $\varepsilon_{pq}^{0(kl)}$ and $\varepsilon_{pq}^{\phi(kl)}$ have been defined in (11) and ε_{ij}^{v} is given by

$$\varepsilon_{ij}^{v} = \frac{1}{2}\left(\frac{\partial v_i}{\partial y_j} + \frac{\partial v_j}{\partial y_i}\right). \tag{14}$$

After standard finite element discretization, the equilibrium equation (7) (as well as its weak form (12)) transforms into

$$\boldsymbol{K}\boldsymbol{\phi} = \boldsymbol{F}, \tag{15}$$

where $\boldsymbol{\phi}$ is Y-periodic, $\boldsymbol{K}$ is the well-known global stiffness matrix in traditional finite element method for solid mechanics,

$$\boldsymbol{K} = \sum_e \int_{Y^e} \boldsymbol{B}^{\top}\boldsymbol{D}\boldsymbol{B}\,\mathrm{d}\boldsymbol{y}, \tag{16}$$

and $\boldsymbol{F}$ is the *pseudo nodal load* given by

$$\boldsymbol{F} = \sum_e \int_{Y^e} \boldsymbol{B}^{\top}\boldsymbol{D}\,\mathrm{d}\boldsymbol{y}. \tag{17}$$

Upon solution of the characteristic function $\boldsymbol{\phi}$, the effective elasticity tensor can be given by

$$\boldsymbol{D}^{\heartsuit} = \frac{1}{|\boldsymbol{Y}|}\sum_e \int_{Y^e} \boldsymbol{D}(\boldsymbol{I} - \boldsymbol{B}\boldsymbol{\phi})\,\mathrm{d}\boldsymbol{y}. \tag{18}$$

From (15) to (18), one can find that the strain–displacement matrix $\boldsymbol{B}$ should be used to form the pseudo nodal loads $\boldsymbol{F}$ and to calculate the effective elastic moduli $\boldsymbol{D}^{\heartsuit}$. Throughout this paper we use the heart suit icon ♡ as a superscript to stand for the homogenized parameters. In general-purpose commercial finite element software, the strain–displacement matrix is usually not available, so it is not easy to calculate the effective elastic moduli by directly taking the commercial finite element software as a black box.

3 Cauchy–Born hypothesis based numerical homogenization

As illustrated in the previous section, the derivation of AH is complicated. In this section we will carry out the detailed work flow of Cauchy–Born rule based numerical homogenization (CBNH for short), which is easy and straightforward to understand and implement. The whole work flow of the CBNH can rely totally on commercial FEA software. On solution of the effective elastic moduli, the deformation modes of the unit cell under different kinds of prescribed strain field can also be obtained at the same time.

3.1 Finding the effective elastic moduli by Cauchy–Born rule based numerical homogenization

Different from the AH method, the CBNH method is based on a *geometrically intuitive* viewpoint of the periodic structures. Using the terminology of solid state physics (Kittel 2005), periodic structures are constructed by the infinite repetition of identical building blocks (see Fig. 1). A building block is called the *basis*. The corner nodes of the basis define the *lattice*, and the lattice is said to be *primitive* if it is the smallest building block of the periodic structures.

The Cauchy–Born rule in solid state physics (Ericksen 2008) states that *the position of the atoms in a crystal lattice follow the overall strain of the medium*. Refer to Fig. 2, let $\boldsymbol{a}^{(\alpha)}$ be the deformed primitive translational vector[1] and $\boldsymbol{A}^{(\alpha)}$ the undeformed one, here $\alpha = 1, 2$ for two-dimensional case

[1] There are alternative names for the vectors $\boldsymbol{a}^{(1)}, \boldsymbol{a}^{(2)}$ in the literature, e.g., bond vector, lattice vector, tessellation vector etc.

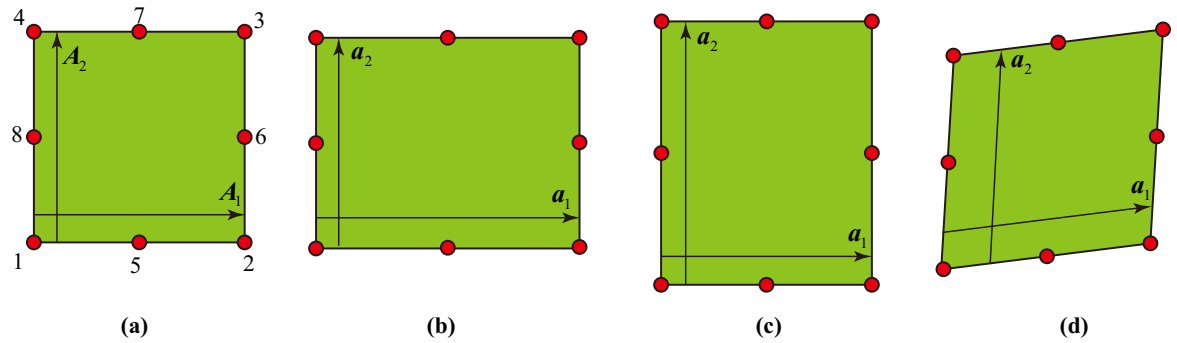

Fig. 2 The unit cell in undeformed and deformed state. **a** undeformed shape. **b** One possible deformed shape for $\boldsymbol{\varepsilon} = \begin{bmatrix} \varepsilon_{11} & 0 \\ 0 & 0 \end{bmatrix}$. **c** One possible deformed shape for $\boldsymbol{\varepsilon} = \begin{bmatrix} 0 & 0 \\ 0 & \varepsilon_{22} \end{bmatrix}$. **d** One possible deformed shape for $\boldsymbol{\varepsilon} = \begin{bmatrix} 0 & \varepsilon_{12} \\ \varepsilon_{12} & 0 \end{bmatrix}$

and $\alpha = 1, 2, 3$ for three-dimensional case. For simplicity all the equations will be given in terms of two-dimensional case, but can be freely generalized to three-dimensional case without any difficulty. Applying the Cauchy–Born rule to the bond vectors leads to (Chandraseker et al. 2006)

$$a_i^{(\alpha)} = \overline{F}_{ij} A_j^{(\alpha)}, \tag{19}$$

where $\overline{F}_{ij}$ is the *prescribed* deformation gradient exerted on the medium. In small deformation regime, Eq. (19) can be rewritten as

$$a_i^{(\alpha)} = (\delta_{ij} + \overline{\varepsilon}_{ij}) A_j^{(\alpha)} = A_i^{(\alpha)} + \overline{\varepsilon}_{ij} A_j^{(\alpha)}, \tag{20}$$

where $\overline{\boldsymbol{\varepsilon}}$ is the *prescribed* infinitesimal strain tensor exerted on the medium,

$$\overline{\boldsymbol{\varepsilon}} = \begin{bmatrix} \overline{\varepsilon}_{11} & \overline{\varepsilon}_{12} \\ \overline{\varepsilon}_{12} & \overline{\varepsilon}_{22} \end{bmatrix}. \tag{21}$$

It follows from (20) that the deformation of the primitive translational vector, denoted by d_i^{α}, can be written as

$$d_i^{(\alpha)} = a_i^{(\alpha)} - A_i^{(\alpha)} = \overline{\varepsilon}_{ij} A_j^{(\alpha)}. \tag{22}$$

Equation (19) reveals that the bond vectors are regarded as infinitesimal line segments in the continuum under the Cauchy–Born rule.

Take the rectangular unit cell as shown in Fig. 2 as an example, it has two orthogonal bond vectors $\boldsymbol{A}^{(1)}$ and $\boldsymbol{A}^{(2)}$ in its undeformed state. The undeformed and deformed bond vectors can be respectively written as

$$\begin{cases} \boldsymbol{A}^{(1)} = \boldsymbol{X}_2 - \boldsymbol{X}_1 = \boldsymbol{X}_6 - \boldsymbol{X}_8 = \boldsymbol{X}_3 - \boldsymbol{X}_4, \\ \boldsymbol{A}^{(2)} = \boldsymbol{X}_4 - \boldsymbol{X}_1 = \boldsymbol{X}_7 - \boldsymbol{X}_5 = \boldsymbol{X}_3 - \boldsymbol{X}_2, \end{cases} \tag{23}$$

and

$$\begin{cases} \boldsymbol{a}^{(1)} = \boldsymbol{x}_2 - \boldsymbol{x}_1 = \boldsymbol{x}_6 - \boldsymbol{x}_8 = \boldsymbol{x}_3 - \boldsymbol{x}_4, \\ \boldsymbol{a}^{(2)} = \boldsymbol{x}_4 - \boldsymbol{x}_1 = \boldsymbol{x}_7 - \boldsymbol{x}_5 = \boldsymbol{x}_3 - \boldsymbol{x}_2, \end{cases} \tag{24}$$

where $\boldsymbol{X}_k$ and $\boldsymbol{x}_k$ are the position vectors of kth boundary node in undeformed and deformed state, respectively.

Subtracting (24) from (23) leads to the deformation of the primitive translational vector,

$$\begin{cases} \boldsymbol{d}^{(1)} = \boldsymbol{u}_2 - \boldsymbol{u}_1 = \boldsymbol{u}_3 - \boldsymbol{u}_4 = \boldsymbol{u}_6 - \boldsymbol{u}_8, \\ \boldsymbol{d}^{(2)} = \boldsymbol{u}_4 - \boldsymbol{u}_1 = \boldsymbol{u}_3 - \boldsymbol{u}_2 = \boldsymbol{u}_7 - \boldsymbol{u}_5, \end{cases} \tag{25}$$

where $\boldsymbol{u}_k = \boldsymbol{x}_k - \boldsymbol{X}_k$ is the displacement of kth node, $\boldsymbol{d}^{(\alpha)}$ is the deformation of the primitive translational vector. Combining (25) and (22) gives *the boundary condition of the unit cell under prescribed strain*,

$$\begin{cases} \boldsymbol{u}_2 - \boldsymbol{u}_1 = \boldsymbol{u}_3 - \boldsymbol{u}_4 = \boldsymbol{u}_6 - \boldsymbol{u}_8 = \overline{\boldsymbol{\varepsilon}} \boldsymbol{A}^{(1)}, \\ \boldsymbol{u}_4 - \boldsymbol{u}_1 = \boldsymbol{u}_3 - \boldsymbol{u}_2 = \boldsymbol{u}_7 - \boldsymbol{u}_5 = \overline{\boldsymbol{\varepsilon}} \boldsymbol{A}^{(2)}. \end{cases} \tag{26}$$

As an example, Fig. 2b–d illustrate the deformed shape of the unit cell under different kinds of prescribed strain field.

Equation (26) acts as the boundary condition of the PUC. The deformation state of the unit cell under a prescribed stain field $\overline{\boldsymbol{\varepsilon}}$ can be found by solving a static equilibrium problem together with the boundary condition (26), which can be done easily in all the commercial finite element software where the boundary condition can be applied through multiple point constraint (MPC for short). Upon solution of the unit cell's displacement field, the *strain energy* of the unit cell can be expressed as

$$\Pi = \frac{1}{2} \boldsymbol{u}^{\top} \boldsymbol{K} \boldsymbol{u}, \tag{27}$$

where $\boldsymbol{u} \in \mathbb{R}^{n_{\text{dof}}}$ is the global displacement vector, $\boldsymbol{K} \in \mathbb{R}^{n_{\text{dof}} \times n_{\text{dof}}}$ is the global stiffness matrix, n_{dof} is the number

of dofs in the finite element model. In all the commercial finite element software, the strain energy Π can be designated as an output variable.

On the other hand, by regarding the PUCs as a homogeneous medium, the strain energy of the unit cell can also be expressed as,

$$\begin{aligned}\Pi &= \int_Y w\,\mathrm{d}\Omega = \int_Y \frac{1}{2} D^{\heartsuit}_{ijkl}\bar{\varepsilon}_{ij}\bar{\varepsilon}_{kl}\,\mathrm{d}\Omega \\ &= \int_Y \frac{1}{2}\underline{\bar{\varepsilon}}^{\top}\boldsymbol{D}^{\heartsuit}\underline{\bar{\varepsilon}}\,\mathrm{d}\Omega = \frac{V}{2}\underline{\bar{\varepsilon}}^{\top}\boldsymbol{D}^{\heartsuit}\underline{\bar{\varepsilon}},\end{aligned} \tag{28}$$

where $w = \frac{1}{2}D^{\heartsuit}_{ijkl}\bar{\varepsilon}_{ij}\bar{\varepsilon}_{kl}$ is the strain energy density, V is the volume of the unit cell, $\bar{\varepsilon}_{ij}$ is the prescribed strain component, $\underline{\bar{\varepsilon}}$ is the Voigt notion of the prescribed strain field

$$\underline{\bar{\varepsilon}} = \begin{bmatrix}\varepsilon_1\\ \varepsilon_2\\ 2\varepsilon_6\end{bmatrix} = \begin{bmatrix}\varepsilon_{11}\\ \varepsilon_{22}\\ 2\varepsilon_{12}\end{bmatrix}, \tag{29}$$

note that in the Cauchy–Born rule the prescribed strain $\bar{\varepsilon}_{ij}$ is assumed to be applied on the medium in the macroscopic level; $\boldsymbol{D}^{\heartsuit}$ is the matrix notion of the effective elastic moduli,

$$\boldsymbol{D}^{\heartsuit} = \begin{bmatrix}D^{\heartsuit}_{11} & D^{\heartsuit}_{12} & D^{\heartsuit}_{16}\\ D^{\heartsuit}_{12} & D^{\heartsuit}_{22} & D^{\heartsuit}_{26}\\ D^{\heartsuit}_{16} & D^{\heartsuit}_{26} & D^{\heartsuit}_{66}\end{bmatrix} = \begin{bmatrix}D^{\heartsuit}_{1111} & D^{\heartsuit}_{1122} & D^{\heartsuit}_{1112}\\ D^{\heartsuit}_{1122} & D^{\heartsuit}_{2222} & D^{\heartsuit}_{2212}\\ D^{\heartsuit}_{1112} & D^{\heartsuit}_{2212} & D^{\heartsuit}_{1212}\end{bmatrix}. \tag{30}$$

Since the prescribed strain field $\underline{\bar{\varepsilon}}$ is known in advance, by equating (27) and (28) the entries of the effective elastic moduli can be calculated through special arrangement of the entries in $\underline{\bar{\varepsilon}}$. For example, by setting $\underline{\bar{\varepsilon}} = [1,0,0]^{\top}$, we have

$$D^{\heartsuit}_{11} = \frac{2}{V}\Pi_{[1,0,0]}, \tag{31}$$

where $\Pi_{[1,0,0]}$ denotes the strain energy under prescribed strain field $\underline{\bar{\varepsilon}} = [1,0,0]^{\top}$. Similarly we can also find the other entries of the effective elastic moduli,

$$\begin{aligned}D^{\heartsuit}_{22} &= \frac{2}{V}\Pi_{[0,1,0]},\\ D^{\heartsuit}_{66} &= \frac{2}{V}\Pi_{[0,0,1]},\\ D^{\heartsuit}_{12} &= \frac{1}{V}\Pi_{[1,1,0]} - \frac{1}{2}\left(D^{\heartsuit}_{11} + D^{\heartsuit}_{22}\right),\\ D^{\heartsuit}_{16} &= \frac{1}{V}\Pi_{[1,0,1]} - \frac{1}{2}\left(D^{\heartsuit}_{11} + D^{\heartsuit}_{66}\right),\\ D^{\heartsuit}_{26} &= \frac{1}{V}\Pi_{[0,1,1]} - \frac{1}{2}\left(D^{\heartsuit}_{22} + D^{\heartsuit}_{66}\right).\end{aligned} \tag{32}$$

Under the boundary condition (26) the displacement field of the unit cell cannot be uniquely determined since the rigid-body displacement has not be constrained. Fortunately the rigid-body displacement makes no contribution to the strain energy (since no strain or stress occurs due to the rigid-body displacement), thus all possible solutions of the unit cell lead to exactly the same effective elastic moduli. It is also possible to fix any node (but only one node can be fixed) so that the displacement field of the unit cell can be uniquely determined.

Now we can summarize the procedure to calculate the effective elastic moduli by means of Cauchy–Born rule based numerical homogenization as follows.

(1) Set up the finite element model (including geometry building, finite element discretization and configuration of the material properties) of the unit cell in the FEA software.

(2) Let $\underline{\bar{\varepsilon}} = [1,0,0]^{\top}$, or equivalently let $\bar{\varepsilon} = \begin{bmatrix}1 & 0\\ 0 & 0\end{bmatrix}$, apply the boundary condition (26) by MPC within the FEA software. Calculate the displacement field, and output the strain energy $\Pi_{[1,0,0]}$. Then $D^{\heartsuit}_{11} = \frac{2}{V}\Pi_{[1,0,0]}$.

(3) Let $\underline{\bar{\varepsilon}} = [0,1,0]^{\top}$, or equivalently let $\bar{\varepsilon} = \begin{bmatrix}0 & 0\\ 0 & 1\end{bmatrix}$, repeat (2) to obtain $\Pi_{[0,1,0]}$. Then $D^{\heartsuit}_{22} = \frac{2}{V}\Pi_{[0,1,0]}$.

(4) Let $\underline{\bar{\varepsilon}} = [0,0,1]^{\top}$, or equivalently let $\bar{\varepsilon} = \begin{bmatrix}0 & 0.5\\ 0.5 & 0\end{bmatrix}$, repeat (2) to obtain $\Pi_{[0,0,1]}$. Then $D^{\heartsuit}_{66} = \frac{2}{V}\Pi_{[0,0,1]}$.

(5) Let $\underline{\bar{\varepsilon}} = [1,1,0]^{\top}$, or equivalently let $\bar{\varepsilon} = \begin{bmatrix}1 & 0\\ 0 & 1\end{bmatrix}$, repeat (2) to obtain $\Pi_{[1,1,0]}$. Then $D^{\heartsuit}_{12} = \frac{1}{V}\Pi_{[1,1,0]} - \frac{1}{2}(D^{\heartsuit}_{11} + D^{\heartsuit}_{22})$.

(6) Let $\underline{\bar{\varepsilon}} = [1,0,1]^{\top}$, or equivalently let $\bar{\varepsilon} = \begin{bmatrix}1 & 0.5\\ 0.5 & 0\end{bmatrix}$, repeat (2) to obtain $\Pi_{[1,0,1]}$. Then $D^{\heartsuit}_{16} = \frac{1}{V}\Pi_{[1,0,1]} - \frac{1}{2}(D^{\heartsuit}_{11} + D^{\heartsuit}_{66})$.

(7) Let $\underline{\bar{\varepsilon}} = [0,1,1]^{\top}$, or equivalently let $\bar{\varepsilon} = \begin{bmatrix}0 & 0.5\\ 0.5 & 1\end{bmatrix}$, repeat (2) to obtain $\Pi_{[0,1,1]}$. Then $D^{\heartsuit}_{26} = \frac{1}{V}\Pi_{[0,1,1]} - \frac{1}{2}(D^{\heartsuit}_{22} + D^{\heartsuit}_{66})$.

As can be found from the procedure shown above, all the steps can be executed within commercial FEA software's built-in functionality. This is the advantage of the Cauchy–Born rule based numerical homogenization method.

3.2 Distinctions between the methods of CBNH and RVE

The concept of RVE plays a vital role in the composite mechanics. The well-known Hill theorem (Aboudi 1991) in composite mechanics states that the homogeneous displacement and traction boundary conditions in the RVE method lead to the upper and lower bounds of the effective moduli, respectively. In composite mechanics textbooks, the upper bound and lower bound are usually called as the Voigt bound and Reuss bound, respectively. Take the Voigt bound as an

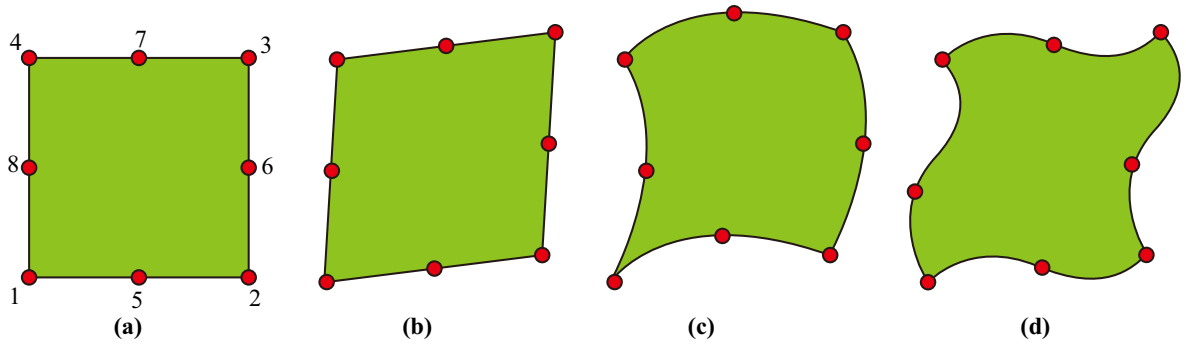

Fig. 3 Different deformation modes under prescribed strain field $\boldsymbol{\varepsilon} = \begin{bmatrix} 0 & \varepsilon_{12} \\ \varepsilon_{12} & 0 \end{bmatrix}$. **a** Original undeformed shape, and **b**–**d** three possible deformed shape. In CBNH, all the modes **b**–**d** are possible, while in the homogeneous displacement boundary condition, only **b** is admissible

example, the *homogeneous displacement boundary condition* is given by

$$u_i(\boldsymbol{y}) = \bar{\varepsilon}_{ij} y_j, \quad \forall \boldsymbol{y} \in \partial \boldsymbol{Y}, \tag{33}$$

where $\bar{\varepsilon}_{ij}$ is the prescribed constant strains. The homogeneous displacement boundary condition is applied to the exterior boundary of the RVE. According to the average strain theorem, the average strain in the RVE is equal to the prescribed constant strain.

As shown in Fig. 3, take the square unit cell as an example. Let $\boldsymbol{A}_1 = [1, 0]^\top$, $\boldsymbol{A}_2 = [0, 1]^\top$ denote the primitive translational vectors, and assume that the origin is located at node 1. Consider the prescribed shear strain $\bar{\boldsymbol{\varepsilon}} = \begin{bmatrix} 0 & 1 \\ 1 & 0 \end{bmatrix}$, the homogeneous boundary condition (33) for all the boundary nodes can be given by

$$\begin{aligned}
&\begin{bmatrix} u_1 \\ v_1 \end{bmatrix} = \begin{bmatrix} 0 \\ 0 \end{bmatrix}, \quad \begin{bmatrix} u_2 \\ v_2 \end{bmatrix} = \begin{bmatrix} 0 \\ 1 \end{bmatrix}, \quad \begin{bmatrix} u_3 \\ v_3 \end{bmatrix} = \begin{bmatrix} 1 \\ 1 \end{bmatrix}, \\
&\begin{bmatrix} u_4 \\ v_4 \end{bmatrix} = \begin{bmatrix} 1 \\ 0 \end{bmatrix}, \quad \begin{bmatrix} u_5 \\ v_5 \end{bmatrix} = \begin{bmatrix} 0 \\ 0.5 \end{bmatrix}, \quad \begin{bmatrix} u_6 \\ v_6 \end{bmatrix} = \begin{bmatrix} 0.5 \\ 1 \end{bmatrix}, \\
&\begin{bmatrix} u_7 \\ v_7 \end{bmatrix} = \begin{bmatrix} 1 \\ 0.5 \end{bmatrix}, \quad \begin{bmatrix} u_8 \\ v_8 \end{bmatrix} = \begin{bmatrix} 0.5 \\ 0 \end{bmatrix},
\end{aligned} \tag{34}$$

where u_i and v_i are the horizontal and vertical displacements of ith node, respectively. In CBNH, the affine boundary condition (26) can be given by

$$\begin{aligned}
&\begin{bmatrix} u_2 - u_1 \\ v_2 - v_1 \end{bmatrix} = \begin{bmatrix} u_3 - u_4 \\ v_3 - v_4 \end{bmatrix} = \begin{bmatrix} u_6 - u_8 \\ v_6 - v_8 \end{bmatrix} = \begin{bmatrix} 0 \\ 1 \end{bmatrix}, \\
&\begin{bmatrix} u_4 - u_1 \\ v_4 - v_1 \end{bmatrix} = \begin{bmatrix} u_3 - u_2 \\ v_3 - v_2 \end{bmatrix} = \begin{bmatrix} u_7 - u_5 \\ v_7 - v_5 \end{bmatrix} = \begin{bmatrix} 1 \\ 0 \end{bmatrix}.
\end{aligned} \tag{35}$$

Compare (34) and (35), one can find that the affine boundary condition in CBNH is in fact a relaxation version of the homogeneous boundary condition in the sense that the latter constrains the absolute value of the displacement of each boundary node while the former only requires the relative displacement values of each node pair on opposite sides to be consistent with the prescribed strain field. In other words, all the deformation modes satisfying (34) would definitely satisfy (35), but not vise versa. As shown in Fig. 3, the deformation modes (b)–(d) all satisfy the affine boundary condition in CBNH, but only (b) satisfies the homogeneous boundary condition. In (b), the originally straight edges still remain straight in the deformation state; in (c) and (d), however, all the edges are curved in the deformation state. It should be noted here that the *straight-remains-straight* boundary conditions in two-dimensional case and *plane-remains-plane* boundary conditions in three-dimensional case are over-constrained, especially under shear loading cases (Xia et al. 2003).

An important remark is that the homogeneous displacement boundary conditions can only lead to the upper bound of the effective moduli. In order to obtain tight bounds of the effective moduli using the homogeneous displacement boundary conditions, the RVE should include as many unit cells as possible (Aboudi 1991), thus rendering the RVE concept not a good choice to calculate the effective moduli of the PUCs when the detailed geometry and material information of the constituents is available (Yan et al. 2006), which is exactly the cases we tackle with in this paper. The comparison between our method and the RVE with homogeneous displacement boundary condition will further be explained by numerical examples in Sect. 4.1.

3.3 Sensitivity analysis

In this subsection we carry out the sensitivity analysis of the Cauchy–Born rule based numerical homogenization procedure, which is needed in inverse homogenization applications. All the equations will be expressed using

matrix notion for convenience. First of all, we need to formulate the affine boundary condition (26) in a more compact form,

$$\begin{bmatrix} -\boldsymbol{I} & \boldsymbol{I} & \boldsymbol{O} & \boldsymbol{O} & \boldsymbol{O} & \boldsymbol{O} & \boldsymbol{O} & \boldsymbol{O} \\ \boldsymbol{O} & \boldsymbol{O} & \boldsymbol{I} & -\boldsymbol{I} & \boldsymbol{O} & \boldsymbol{O} & \boldsymbol{O} & \boldsymbol{O} \\ \boldsymbol{O} & \boldsymbol{O} & \boldsymbol{O} & \boldsymbol{O} & \boldsymbol{O} & \boldsymbol{I} & \boldsymbol{O} & -\boldsymbol{I} \\ -\boldsymbol{I} & \boldsymbol{O} & \boldsymbol{O} & \boldsymbol{I} & \boldsymbol{O} & \boldsymbol{O} & \boldsymbol{O} & \boldsymbol{O} \\ \boldsymbol{O} & -\boldsymbol{I} & \boldsymbol{I} & \boldsymbol{O} & \boldsymbol{O} & \boldsymbol{O} & \boldsymbol{O} & \boldsymbol{O} \\ \boldsymbol{O} & \boldsymbol{O} & \boldsymbol{O} & \boldsymbol{O} & -\boldsymbol{I} & \boldsymbol{O} & \boldsymbol{I} & \boldsymbol{O} \end{bmatrix} \begin{bmatrix} \boldsymbol{u}_1 \\ \boldsymbol{u}_2 \\ \boldsymbol{u}_3 \\ \boldsymbol{u}_4 \\ \boldsymbol{u}_5 \\ \boldsymbol{u}_6 \\ \boldsymbol{u}_7 \\ \boldsymbol{u}_8 \end{bmatrix} = \begin{bmatrix} \bar{\boldsymbol{\varepsilon}}\boldsymbol{A}^{(1)} \\ \bar{\boldsymbol{\varepsilon}}\boldsymbol{A}^{(1)} \\ \bar{\boldsymbol{\varepsilon}}\boldsymbol{A}^{(1)} \\ \bar{\boldsymbol{\varepsilon}}\boldsymbol{A}^{(2)} \\ \bar{\boldsymbol{\varepsilon}}\boldsymbol{A}^{(2)} \\ \bar{\boldsymbol{\varepsilon}}\boldsymbol{A}^{(2)} \end{bmatrix}. \tag{36}$$

Note that since $\boldsymbol{u}_i$ are of dimension 2×1, the submatrices $\boldsymbol{I}$ and $\boldsymbol{O}$ in (36) are of dimension 2×2,

$$\boldsymbol{I} = \begin{bmatrix} 1 & 0 \\ 0 & 1 \end{bmatrix}, \quad \boldsymbol{O} = \begin{bmatrix} 0 & 0 \\ 0 & 0 \end{bmatrix}. \tag{37}$$

For short, we rewrite (36) as

$$\boldsymbol{P}_{\mathrm{E}}\boldsymbol{u}_{\mathrm{E}} = \boldsymbol{q}, \tag{38}$$

where the meaning of $\boldsymbol{P}_{\mathrm{E}}$, $\boldsymbol{u}_{\mathrm{E}}$ and $\boldsymbol{q}$ are obvious by comparing (36) and (38). $\boldsymbol{u}_{\mathrm{E}} = [\boldsymbol{u}_1, \boldsymbol{u}_2, \ldots, \boldsymbol{u}_8]^{\top}$ corresponds to the displacement of the exterior boundary nodes, so it can be expressed using the global displacement vector $\boldsymbol{u} \in \mathbb{R}^{n_{\mathrm{dof}}}$ as

$$\boldsymbol{u}_{\mathrm{E}} = \boldsymbol{L}\boldsymbol{u}, \tag{39}$$

where $\boldsymbol{L}$ is a mapping matrix with $L_{ij} = 1$ when the $u_{\mathrm{E}i}$ coincides with u_j and $L_{ij} = 0$ otherwise. Let n_{E} denote the number of exterior boundary nodes and n_{C} denote the number of constraints in (36), then in two-dimensional case $\boldsymbol{u}_{\mathrm{E}} \in \mathbb{R}^{2n_{\mathrm{E}}}$, $\boldsymbol{q} \in \mathbb{R}^{n_{\mathrm{C}}}$, $\boldsymbol{P}_{\mathrm{E}} \in \mathbb{R}^{n_{\mathrm{C}} \times 2n_{\mathrm{E}}}$ and $\boldsymbol{L} \in [0,1]^{2n_{\mathrm{E}} \times n_{\mathrm{dof}}}$.

Substituting (39) into (38) leads to

$$\boldsymbol{P}\boldsymbol{u} = \boldsymbol{q}, \tag{40}$$

where $\boldsymbol{P} = \boldsymbol{P}_{\mathrm{E}}\boldsymbol{L} \in \mathbb{R}^{n_{\mathrm{C}} \times n_{\mathrm{dof}}}$. It is obvious that only a small portion of entries in $\boldsymbol{P}$ are nonzero, thus $\boldsymbol{P}$ may be conveniently written as a sparse matrix. We note here that $\boldsymbol{P}$ depends on the layout of the unit cell, so should be specified by the users during the sensitivity analysis.

In order to find the displacement field of the unit cell under a prescribed strain field, the static equilibrium equation should be solved along with the boundary condition (40). We use the Lagrange multiplier approach to deal with the boundary condition. The potential energy (which is equal to the strain energy since no body force or surface traction is considered) of the unit cell is given by

$$\Pi = \frac{1}{2}\boldsymbol{u}^{\top}\boldsymbol{K}\boldsymbol{u} + \lambda^{\top}(\boldsymbol{P}\boldsymbol{u} - \boldsymbol{q}), \tag{41}$$

where $\boldsymbol{K} \in \mathbb{R}^{n_{\mathrm{dof}} \times n_{\mathrm{dof}}}$ is the global stiffness matrix, $\lambda \in \mathbb{R}^{n_{\mathrm{dof}}}$ is an arbitrarily chosen Lagrange multiplier. According to the minimum total strain energy principle, the true displacement of a system would minimizes the total potential. Thus to find the true displacement field, we seek to solve the extremum condition,

$$\delta\Pi = 0 \Rightarrow \begin{cases} \Pi_{\boldsymbol{u}} = \boldsymbol{K}\boldsymbol{u} + \boldsymbol{P}^{\top}\lambda = \boldsymbol{0}, \\ \Pi_{\lambda} = \boldsymbol{P}\boldsymbol{u} - \boldsymbol{q} = \boldsymbol{0}. \end{cases} \tag{42}$$

Equation (42) can be written in a more compact form,

$$\widetilde{\boldsymbol{K}}\widetilde{\boldsymbol{U}} = \widetilde{\boldsymbol{F}}, \tag{43}$$

where

$$\widetilde{\boldsymbol{K}} = \begin{bmatrix} \boldsymbol{K} & \boldsymbol{P}^{\top} \\ \boldsymbol{P} & \boldsymbol{0} \end{bmatrix}, \quad \widetilde{\boldsymbol{U}} = \begin{bmatrix} \boldsymbol{u} \\ \lambda \end{bmatrix}, \quad \widetilde{\boldsymbol{F}} = \begin{bmatrix} \boldsymbol{0} \\ \boldsymbol{q} \end{bmatrix}.$$

Equation (43) is the state equation of the Cauchy–Born rule based numerical homogenization procedure.

Now we use the adjoint approach to calculate the sensitivity of the strain energy. Let $\boldsymbol{\xi}$ denote the design variable, then the strain energy can be expressed as

$$\begin{aligned} \Psi(\boldsymbol{u}, \lambda, \boldsymbol{\xi}) = {} & \frac{1}{2}\boldsymbol{u}^{\top}\boldsymbol{K}(\boldsymbol{\xi})\boldsymbol{u} + \boldsymbol{\mu}_{\boldsymbol{u}}^{\top}\left[\boldsymbol{K}(\boldsymbol{\xi})\boldsymbol{u} + \boldsymbol{P}^{\top}\lambda\right] \\ & + \boldsymbol{\mu}_{\lambda}^{\top}(\boldsymbol{P}\boldsymbol{u} - \boldsymbol{q}), \end{aligned} \tag{44}$$

where $\boldsymbol{\mu}_{\boldsymbol{u}} \in \mathbb{R}^{n_{\mathrm{dof}}}$ and $\boldsymbol{\mu}_{\lambda} \in \mathbb{R}^{n_{\mathrm{C}}}$ are the Lagrange multipliers corresponding to $\Pi_{\boldsymbol{u}}$ and Π_{λ}, respectively. Differentiating $\Psi(\boldsymbol{u}, \lambda, \boldsymbol{\xi})$ w.r.t. ξ_i gives,

$$\begin{aligned} \frac{\partial \Psi}{\partial \xi_i} = {} & \frac{1}{2}\boldsymbol{u}^{\top}\frac{\partial \boldsymbol{K}}{\partial \xi_i}\boldsymbol{u} + \boldsymbol{u}^{\top}\boldsymbol{K}\frac{\partial \boldsymbol{u}}{\partial \xi_i} \\ & + \boldsymbol{\mu}_{\boldsymbol{u}}^{\top}\left(\frac{\partial \boldsymbol{K}}{\partial \xi_i}\boldsymbol{u} + \boldsymbol{K}\frac{\partial \boldsymbol{u}}{\partial \xi_i} + \boldsymbol{P}^{\top}\frac{\partial \lambda}{\partial \xi_i}\right) \\ & + \boldsymbol{\mu}_{\lambda}^{\top}\boldsymbol{P}\frac{\partial \boldsymbol{u}}{\partial \xi_i} \\ = {} & \left(\frac{1}{2}\boldsymbol{u}^{\top}\frac{\partial \boldsymbol{K}}{\partial \xi_i}\boldsymbol{u} + \boldsymbol{\mu}_{\boldsymbol{u}}^{\top}\frac{\partial \boldsymbol{K}}{\partial \xi_i}\boldsymbol{u}\right) \\ & + \left(\boldsymbol{u}^{\top}\boldsymbol{K} + \boldsymbol{\mu}_{\boldsymbol{u}}^{\top}\boldsymbol{K} + \boldsymbol{\mu}_{\lambda}^{\top}\boldsymbol{P}\right)\frac{\partial \boldsymbol{u}}{\partial \xi_i} \\ & + \boldsymbol{\mu}_{\boldsymbol{u}}^{\top}\boldsymbol{P}^{\top}\frac{\partial \lambda}{\partial \xi_i}. \end{aligned} \tag{45}$$

In the light of the adjoint approach, Eq. (45) can be simplified if it is required that

$$\begin{cases} \boldsymbol{K}\boldsymbol{\mu}_{\boldsymbol{u}} + \boldsymbol{P}^{\top}\boldsymbol{\mu}_{\lambda} = -\boldsymbol{K}\boldsymbol{u}, \\ \boldsymbol{P}\boldsymbol{\mu}_{\boldsymbol{u}} = \boldsymbol{0}, \end{cases} \tag{46}$$

which can be rewritten as

$$\begin{bmatrix} \boldsymbol{K} & \boldsymbol{P}^{\top} \\ \boldsymbol{P} & \boldsymbol{0} \end{bmatrix}\begin{bmatrix} \boldsymbol{\mu}_{\boldsymbol{u}} \\ \boldsymbol{\mu}_{\lambda} \end{bmatrix} = \begin{bmatrix} -\boldsymbol{K}\boldsymbol{u} \\ \boldsymbol{0} \end{bmatrix}. \tag{47}$$

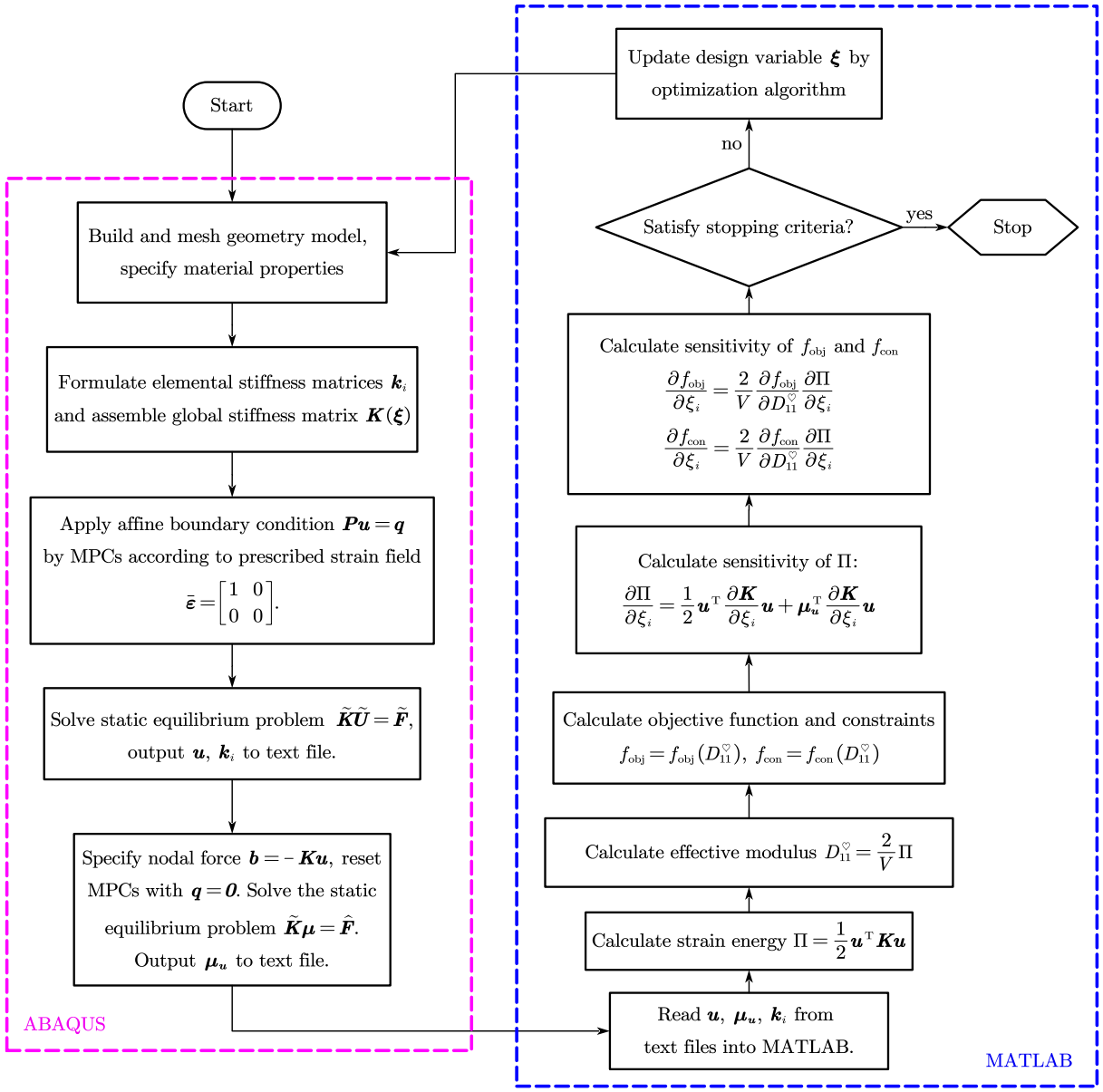

Fig. 4 Flowchart of the inverse homogenization process

Thus the Lagrange multiplier $\boldsymbol{\mu}$ can be found by solving the linear system

$$\widetilde{\boldsymbol{K}}\boldsymbol{\mu} = \hat{\boldsymbol{F}}, \tag{48}$$

where

$$\boldsymbol{\mu} = \begin{bmatrix} \boldsymbol{\mu}_u \\ \boldsymbol{\mu}_\lambda \end{bmatrix}, \quad \hat{\boldsymbol{F}} = \begin{bmatrix} -\boldsymbol{K}\boldsymbol{u} \\ \boldsymbol{0} \end{bmatrix}. \tag{49}$$

It is interesting to find that the left hand side matrix $\widetilde{\boldsymbol{K}}$ coincides with that in the state equation (43), implying that (48) can also be solved within commercial FEA software by specifying $\boldsymbol{b} = -\boldsymbol{K}\boldsymbol{u}$ as the nodal force and resetting all the MPCs with $\boldsymbol{q} = \boldsymbol{0}$.

Substituting (46) into (45) leads to the desired sensitivity result,

$$\frac{\partial \Psi}{\partial \xi_i} = \frac{1}{2}\boldsymbol{u}^{\top}\frac{\partial \boldsymbol{K}}{\partial \xi_i}\boldsymbol{u} + \boldsymbol{\mu}_{\boldsymbol{u}}^{\top}\frac{\partial \boldsymbol{K}}{\partial \xi_i}\boldsymbol{u}, \tag{50}$$

where $\boldsymbol{\mu}_{\boldsymbol{u}}$ can be obtained from (47) or (48), $\partial \boldsymbol{K}/\partial \xi_i$ is determined by the topology optimization method.

3.4 Summary of the CBNH method

In Fig. 4 we show the flowchart of the whole inverse homogenization process. The left parts (i.e., steps within pink lines) refer to the work done by FEA solver (e.g. ABAQUS) while the right parts (i.e., steps within blue lines) refer to the work done by optimization solver (e.g. MATLAB). The detailed workflow of the CBNH method for solving the inverse homogenization problems is outlined as follows. Here we take ABAQUS as the FEA solver and MATLAB as the optimization solver, other choices are possible. Also, for simplicity, we assume that the objective function is only related to $D_{11}^{\heartsuit}$.

(1) In ABAQUS, sequentially execute the following steps.

(i) Build the geometry model and discretize it with finite element meshes, specify material properties. In density based topology optimization methods, usually the elemental fictitious density will be taken as the design variable $\boldsymbol{\xi}$ and the Young's modulus of ith element E_i, would be directly influenced by the ith design variable ξ_i. Cf. Eq. (79) for detailed explanation.

(ii) Formulate elemental stiffness matrices $\boldsymbol{k}_i$ and assemble the global stiffness matrix $\boldsymbol{K}$. Note that this step will automatically be done by ABAQUS during the solving procedure.

(iii) Apply affine boundary conditions $\boldsymbol{Pu} = \boldsymbol{q}$ by MPCs [cf. Eqs. (26), (36) to (40)]. In ABAQUS this can be done with the keyword *Equation*.

(iv) Solve the static equilibrium problem $\widetilde{\boldsymbol{K}}\widetilde{\boldsymbol{U}} = \widetilde{\boldsymbol{F}}$ [cf. Eq. (43)]. Here $\boldsymbol{K}$ is a function of the design variable while the affine boundary condition is considered in $\widetilde{\boldsymbol{F}}$. After solution of the static equilibrium problem, output the displacement field $\boldsymbol{u}$, elemental stiffness matrices $\boldsymbol{k}_i$ to a text file so that such information can be read into MATLAB for the computation of objective function value.

(v) In preparation of sensitivity analysis, another adjoint simulation should be executed within ABAQUS. Specify nodal force vector $\boldsymbol{b} = -\boldsymbol{Ku}$, and reset the affine boundary conditions with $\boldsymbol{q} = 0$. Solve the equilibrium problem $\widetilde{\boldsymbol{K}}\boldsymbol{\mu} = \hat{\boldsymbol{F}}$ [cf. Eq. (48)] to obtain the adjoint solution $\boldsymbol{\mu}_{\boldsymbol{u}}$. Output the $\boldsymbol{\mu}_{\boldsymbol{u}}$ to a text file.

(2) In MATLAB, sequentially execute the following steps.

(i) Read $\boldsymbol{u}$, $\boldsymbol{\mu}_{\boldsymbol{u}}$ and $\boldsymbol{k}_i$ from the text files into MATLAB.

(ii) Calculate strain energy $\Pi = \frac{1}{2}\boldsymbol{u}^{\top}\boldsymbol{Ku}$, or equivalently $\Pi = \frac{1}{2}\sum_{i=1}^{n}\boldsymbol{u}_i^{\top}\boldsymbol{k}_i\boldsymbol{u}_i$. Here n is the number of finite elements, $\boldsymbol{u}_i$ is the displacement vector of ith element, $\boldsymbol{k}_i$ is the elemental stiffness matrix of ith element.

(iii) Calculate the effective modulus $D_{11}^{\heartsuit} = \frac{1}{V}\Pi$. Here only $D_{11}^{\heartsuit}$ is considered for saving space, the extension to other moduli is trivial.

(iv) Calculate the objective function and constraint values, $f_{\text{obj}} = f_{\text{obj}}(D_{11}^{\heartsuit})$, $f_{\text{con}} = f_{\text{con}}(D_{11}^{\heartsuit})$.

(v) Calculate the sensitivity of f_{obj} and f_{con} by the chaining rule,

$$\frac{\partial f_{\text{obj}}}{\partial \xi_i} = \frac{2}{V}\frac{\partial f_{\text{obj}}}{\partial D_{11}^{\heartsuit}}\frac{\partial \Pi}{\partial \xi_i},$$
$$\frac{\partial f_{\text{con}}}{\partial \xi_i} = \frac{2}{V}\frac{\partial f_{\text{con}}}{\partial D_{11}^{\heartsuit}}\frac{\partial \Pi}{\partial \xi_i}.$$

(vi) Check if the stopping criteria are satisfied. Here two kinds of stopping criteria are considered. First, the rule of maximum iterations is checked. If the number of iterations exceed the maximum allowable iterations, the optimization process would stop. Second, the KKT tolerance is checked. If the KKT condition (Nocedal and Wright 2006), a widely used condition to judge whether the current design variables get close the local optimum, is satisfied within prescribed precision, the optimization process would stop. We note here that, the KKT condition in general involves the gradient of the objective function and Jacobian of the constraint, so should be subsequent to the sensitivity analysis.

(vii) If either the rule of maximum iterations or the KKT condition is satisfied, the inverse design process stops. Otherwise, a new design $\boldsymbol{\xi}^{(k+1)}$ is generated by the optimization algorithm (e.g. the *fmincom* function in MATLAB).

(viii) Go to Step (1).

As can be seen from Fig. 4, in the Cauchy–Born rule based inverse homogenization process all the information can be available from commercial FEA software, making it much easier to implement when compared with traditional asymptotic expansion based inverse homogenization process where $\boldsymbol{B}$ matrix plays a key role. In order to facilitate the readers with the usage of the proposed CBNH method, we offer some sample codes as the Supplementary Material. In the sample codes, we use ABAQUS as the FEA solver and the *fmincon* function in MATLAB is used as the optimization solver. More specifically, we use the interior-point algorithm in the *fmincon* function as the optimization algorithm. Data exchange between ABAQUS and MATLAB is accomplished with text files.

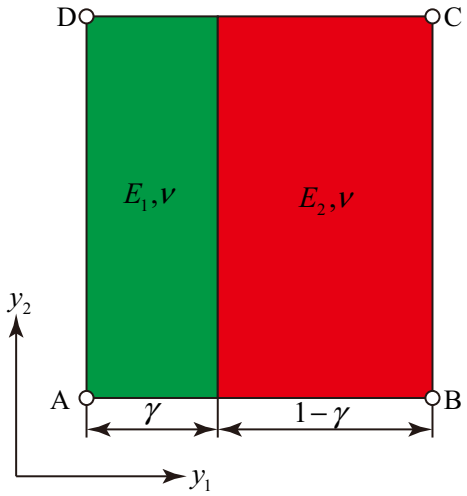

Fig. 5 A rank-1 composite material

4 Numerical examples for homogenization of periodic unit cells

In this section we illustrate the accuracy of the proposed Cauchy–Born rule based numerical homogenization (CBNH for short) method for the calculation of effective elastic moduli. Several examples will be presented successively including both continuum and discrete unit cells. We use linear quadrilateral (two-dimensional cases) or hexagonal (three-dimensional cases) elements with Wilson's incompatible interpolation terms (Ibrahimbegovic and Wilson 1991) to discretize the continuum, this kind of elements are found to be accurate and efficient in our past studies. In Sect. 4.4, linear truss elements will be used. In all the two-dimensional examples, plane stress assumptions are made.

4.1 Rank-1 layered composite

As shown in Fig. 5, we consider a rank-1 composite material comprising of two different isotropic materials. The primitive translational vectors in this case are

$$\boldsymbol{a}^{(1)} = \begin{bmatrix} 1 \\ 0 \end{bmatrix}, \quad \boldsymbol{a}^{(2)} = \begin{bmatrix} 0 \\ m \end{bmatrix}, \tag{51}$$

where m can be an arbitrary positive number since in y_2 direction both constituents extend to infinity. The volume fraction of the first (with Young's modulus E_1 and Poisson's ratio ν) and second constituent (E_2 and ν) are γ and $1-\gamma$, respectively. The affine boundary condition in this example are given as follows,

$$\begin{aligned} \boldsymbol{u}_{\mathrm{B}} &= \boldsymbol{u}_{\mathrm{A}} + \bar{\boldsymbol{\varepsilon}}\boldsymbol{a}^{(1)}, \\ \boldsymbol{u}_{\mathrm{D}} &= \boldsymbol{u}_{\mathrm{A}} + \bar{\boldsymbol{\varepsilon}}\boldsymbol{a}^{(2)}, \\ \boldsymbol{u}_{\mathrm{C}} &= \boldsymbol{u}_{\mathrm{A}} + \bar{\boldsymbol{\varepsilon}}(\boldsymbol{a}^{(1)} + \boldsymbol{a}^{(2)}), \\ \boldsymbol{u}_{(\mathrm{BC})} &= \boldsymbol{u}_{(\mathrm{AD})} + \bar{\boldsymbol{\varepsilon}}\boldsymbol{a}^{(1)}, \\ \boldsymbol{u}_{(\mathrm{DC})} &= \boldsymbol{u}_{(\mathrm{AB})} + \bar{\boldsymbol{\varepsilon}}\boldsymbol{a}^{(2)}, \end{aligned} \tag{52}$$

where (BC) stands for the node set including all the nodes in the interior of edge BC (without the corner nodes B and C); (AD), (DC) and (AB) follow the same way. In order to apply the affine boundary condition (52), the number of nodes on edges AD and BC should be the same, so should edges AB and DC. Among all the boundary nodes, only the corner node A, edge nodes (AB) and (AD) are independent, the displacement of all the other boundary nodes can be calculated through the boundary condition (52). In FEA software the affine boundary condition (52) can be easily applied using the functionality of *Multi-point constraints*, in home-made codes the boundary condition can be implemented with Lagrange multiplier approach.

The effective elastic moduli for rank-1 composite material has analytical expressions (Hassani and Hinton 1998a),

$$\boldsymbol{D}^{\heartsuit} = \begin{bmatrix} I_1 & \nu I_1 & 0 \\ \nu I_1 & I_2 + \nu^2 I_1 & 0 \\ 0 & 0 & \frac{1-\nu}{2} I_1 \end{bmatrix}, \tag{53}$$

where

$$\begin{aligned} I_1 &= \frac{1}{1-\nu^2} \frac{E_1 E_2}{\gamma E_2 + (1-\gamma) E_1}, \\ I_2 &= \gamma E_1 + (1-\gamma) E_2. \end{aligned} \tag{54}$$

Let $E_1 = 100$, $E_2 = 1$, $\nu = 0.3$, Fig. 6 compares the nonzero components of the effective elastic moduli calculated by the proposed CBNH method, the analytical expression (53), and the RVE method with homogeneous displacement boundary condition for different values of γ. As can be found from Fig. 6, the results calculated by the proposed CBNH method agree perfectly with that by analytical expression, demonstrating the effectiveness of the proposed method. On the other hand, the RVE method with homogeneous displacement boundary condition cannot give accurate prediction on all the elastic moduli except for D_{22}. For all the calculated elastic moduli, the results by RVE method are larger than the ones by CBNH and analytical expressions, which is reasonable due to the fact that homogeneous displacement boundary condition leads to upper bounds of elastic moduli (Aboudi 1991). More specifically, Table 1 gives the calculated effective elastic moduli when $\gamma = 0.5$, which clearly

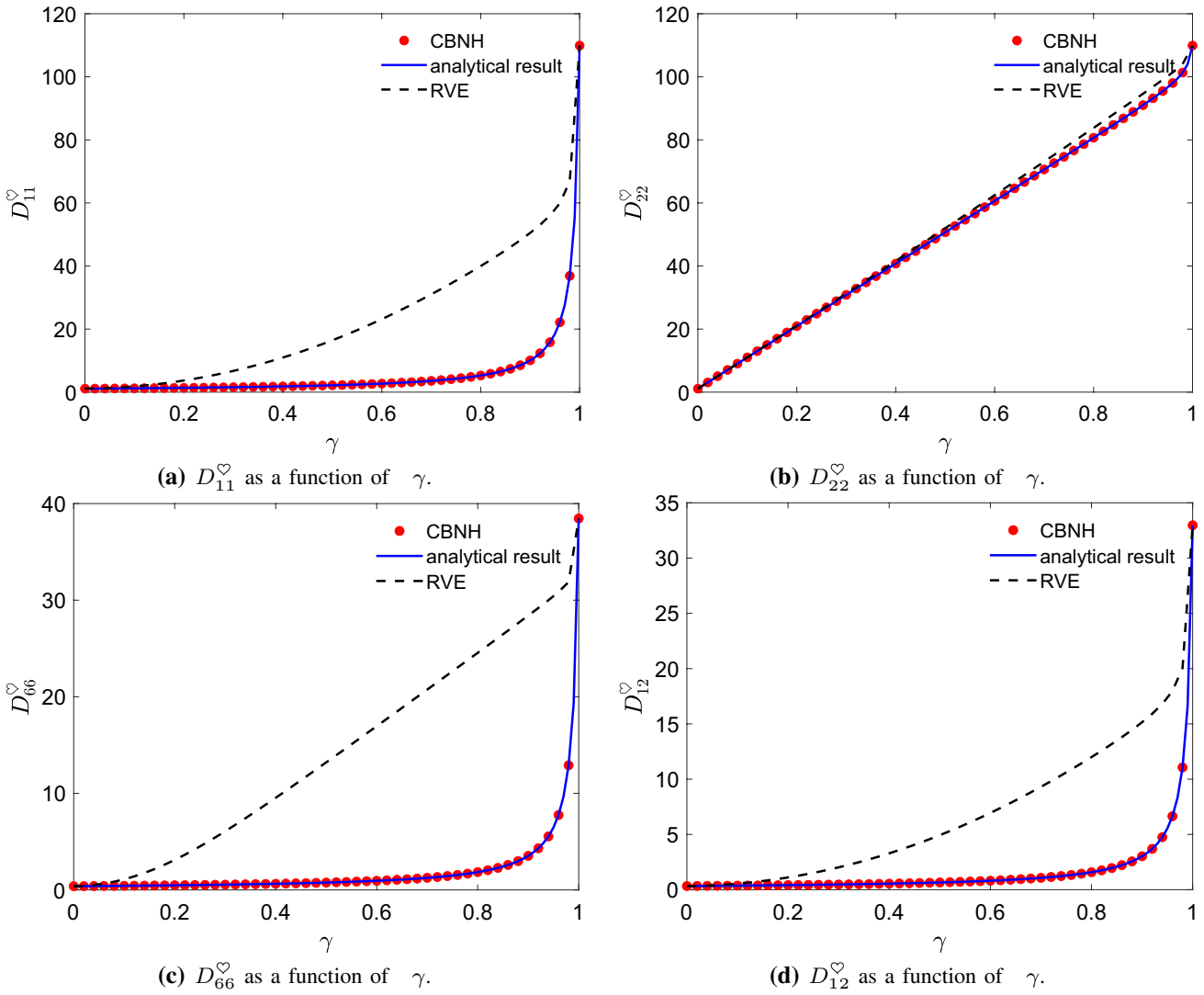

(a) $D_{11}^{\heartsuit}$ as a function of γ.

(b) $D_{22}^{\heartsuit}$ as a function of γ.

(c) $D_{66}^{\heartsuit}$ as a function of γ.

(d) $D_{12}^{\heartsuit}$ as a function of γ.

Fig. 6 Comparisons between CBNH and analytical results

Table 1 Effective elastic moduli of the rank-1 composite material

	$D_{11}^{\heartsuit}$	$D_{22}^{\heartsuit}$	$D_{66}^{\heartsuit}$	$D_{26}^{\heartsuit}$	$D_{16}^{\heartsuit}$	$D_{12}^{\heartsuit}$
CBNH	2.1760	50.6958	0.7616	0	0	0.6528
Equation (53)	2.1760	50.6958	0.7616	0	0	0.6528
RVE	16.4357	51.9792	13.2067	0	0	4.9307

shows the perfect matching between the results calculated by CBNH and the analytical expression. On the contrary, the $D_{11}^{\heartsuit}$, $D_{66}^{\heartsuit}$, $D_{12}^{\heartsuit}$ calculated by RVE method deviates a lot from the known analytical results. Figures 7 and 8 depict the deformed shape of the unit cell under different kinds of prescribed strain field in the proposed CBNH method and the RVE method, respectively. It can be found that the deformation of the unit cell is obviously not linearly dependent on the coordinates under prescribed shear strain in the proposed CBNH method (see the upper and lower edges in Fig. 7c, e, f), but the *relative* displacements between nodes on opposite sides are always consistent with the prescribed strain field. In the RVE method, however, the deformation of the RVE is required to be linearly dependent on the coordinates. It follows that the RVE method with homogeneous displacement boundary condition seems to be *stiffer* than the affine boundary condition in the proposed CBNH method, this complies with the larger calculated effective elastic moduli.

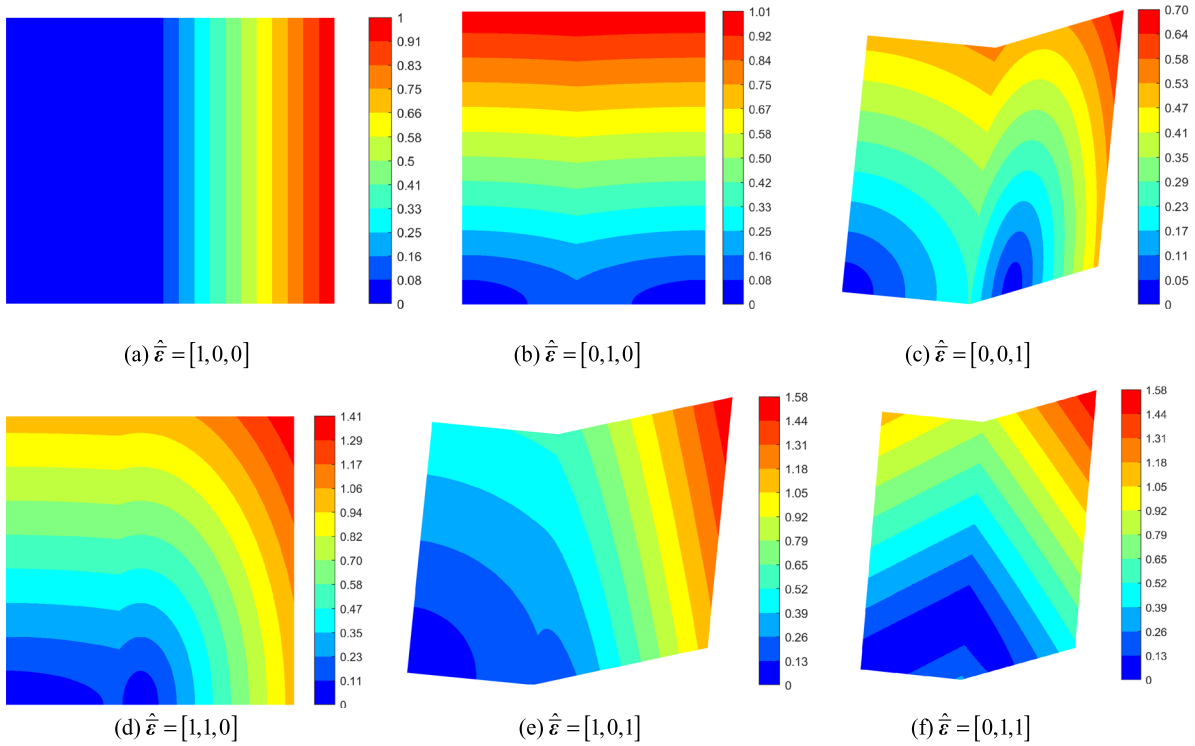

Fig. 7 Deformed shape of the unit cell under different kinds of prescribed strain field in the proposed CBNH method

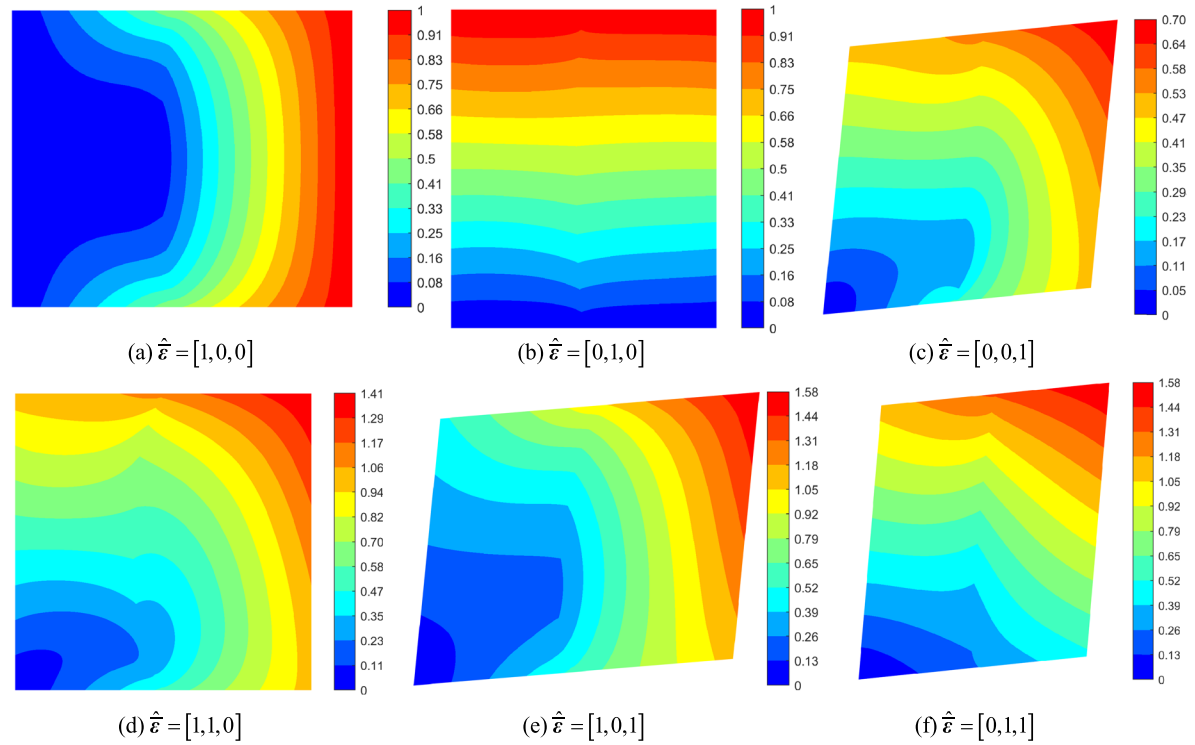

Fig. 8 Deformed shape of the unit cell under different kinds of prescribed strain field in the RVE method

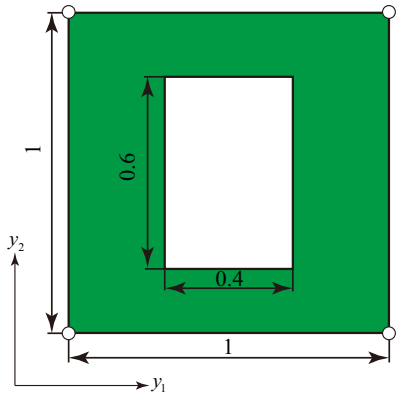

Fig. 9 Unit square base cell with a rectangular hole

4.2 Square base cell with rectangular hole

As shown in Fig. 9, in this example we consider a unit square base cell with a 0.4×0.6 rectangular hole. The solid phase is filled with orthotropic material, $D_{11} = D_{22} = 30$, $D_{12} = D_{66} = 10$, other components are all zero. In this case the primitive translational vectors are

$$\boldsymbol{a}^{(1)} = \begin{bmatrix} 1 \\ 0 \end{bmatrix}, \quad \boldsymbol{a}^{(2)} = \begin{bmatrix} 0 \\ 1 \end{bmatrix}. \tag{55}$$

The boundary condition in this example is exactly the same as that in Sect. 4.1, so will be omitted here.

In Table 2 we compare the effective elastic moduli calculated by CBNH and AH, where AH-1 (Bendsoe and Kikuchi 1988) and AH-2 (Hassani and Hinton 1998a) are the results coming from the literature while AH-3 comes from our home-made asymptotic expansion based homogenization code. In CBNH and AH-3, the FEA model parameters (e.g., number of elements, element type, element size, etc.) are all the same. It is interesting to find that, the effective elastic moduli calculated by CBNH and AH-3 agree very well, while both of them differ a little bit from AH-1 and AH-2 coming from the literature. This implies that the minor discrepancies between our results and that in the literature are possibly caused by the different choices of element shape functions and the number of finite elements to discretize the material domain.

4.3 Hexagonal base cell with voids

As shown in Fig. 10 we consider the honeycomb-like hexagonal unit cell in this example. The edge length is $m = 6$, the thickness is $t = \sqrt{3}$. Note that the thickness of each unit cell is only half the thickness of the honeycomb. The primitive translational vectors are

$$\boldsymbol{a}^{(1)} = \frac{m}{2}\begin{bmatrix} 3 \\ \sqrt{3} \end{bmatrix}, \quad \boldsymbol{a}^{(2)} = \frac{m}{2}\begin{bmatrix} 3 \\ -\sqrt{3} \end{bmatrix}. \tag{56}$$

If we choose corner nodes A and F, edge nodes (AB), (AF) and (FE) as the independent nodes, the boundary conditions can be written as

$$\begin{aligned} \boldsymbol{u}_{\mathrm{B}} &= \boldsymbol{u}_{\mathrm{F}} + \bar{\boldsymbol{\varepsilon}}\boldsymbol{a}^{(2)}, \\ \boldsymbol{u}_{\mathrm{C}} &= \boldsymbol{u}_{\mathrm{A}} + \bar{\boldsymbol{\varepsilon}}\boldsymbol{a}^{(1)}, \\ \boldsymbol{u}_{\mathrm{D}} &= \boldsymbol{u}_{\mathrm{F}} + \bar{\boldsymbol{\varepsilon}}\boldsymbol{a}^{(1)}, \\ \boldsymbol{u}_{\mathrm{E}} &= \boldsymbol{u}_{\mathrm{A}} + \bar{\boldsymbol{\varepsilon}}(\boldsymbol{a}^{(1)} - \boldsymbol{a}^{(2)}), \end{aligned} \tag{57}$$

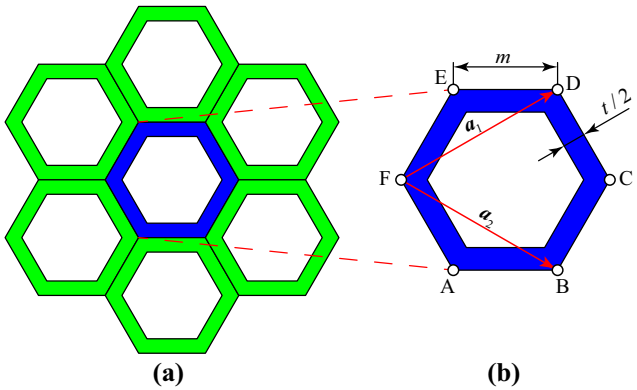

Fig. 10 Hexagonal base shell with voids. **a** Periodic tessellation of unit cells, and **b** one unit cell

Table 2 Effective elastic moduli of the perforated square unit cell as shown in Fig. 9

	$D_{11}^{\heartsuit}$	$D_{22}^{\heartsuit}$	$D_{66}^{\heartsuit}$	$D_{26}^{\heartsuit}$	$D_{16}^{\heartsuit}$	$D_{12}^{\heartsuit}$
CBNH	12.858	17.435	2.663	0	0	3.149
AH-1 (Bendsoe and Kikuchi 1988)	12.844	17.421	2.668	0	0	3.131
AH-2 (Hassani and Hinton 1998a)	12.839	17.422	2.648	0	0	3.139
AH-3	12.858	17.435	2.663	0	0	3.149

Table 3 Effective elastic moduli of the perforated hexagonal unit cell as shown in Fig. 10

	$D^{\heartsuit}_{11}$	$D^{\heartsuit}_{22}$	$D^{\heartsuit}_{66}$	$D^{\heartsuit}_{26}$	$D^{\heartsuit}_{16}$	$D^{\heartsuit}_{12}$
CBNH	0.0969	0.0969	0.0125	0	0	0.0720
AH-1 (Guedes and Kikuchi 1990)	0.0968	0.0968	0.0124	0	0	0.0720
AH-2 (Hassani and Hinton 1998a)	0.0966	0.0966	0.0123	0	0	0.0720

$$\begin{aligned} \boldsymbol{u}_{(\mathrm{BC})} &= \boldsymbol{u}_{(\mathrm{FE})} + \bar{\boldsymbol{\varepsilon}}\boldsymbol{a}^{(2)}, \\ \boldsymbol{u}_{(\mathrm{CD})} &= \boldsymbol{u}_{(\mathrm{AF})} + \bar{\boldsymbol{\varepsilon}}\boldsymbol{a}^{(1)}, \\ \boldsymbol{u}_{(\mathrm{ED})} &= \boldsymbol{u}_{(\mathrm{AB})} + \bar{\boldsymbol{\varepsilon}}(\boldsymbol{a}^{(1)} - \boldsymbol{a}^{(2)}). \end{aligned} \tag{58}$$

In Table 3 we compare the effective elastic moduli calculated by the proposed CBNH method and the traditional AH method, where AH-1 (Guedes and Kikuchi 1990) and AH-2 (Hassani and Hinton 1998a) are the results coming from the literature. The three rows in Table 3 agree very well, revealing that the proposed CBNH method can safely act as an alternative to the currently prevailing AH method. By the way, we mention here that the honeycomb-like PUCs belong to the macroscopically isotropic material, so if computed correctly, the components of the effective elastic moduli should satisfy the isotropy constraint,

$$\begin{aligned} D^{\heartsuit}_{11} &= D^{\heartsuit}_{22}, \\ D^{\heartsuit}_{12} &= D^{\heartsuit}_{11} - 2D^{\heartsuit}_{66}, \\ D^{\heartsuit}_{16} &= D^{\heartsuit}_{26} = 0. \end{aligned} \tag{59}$$

The readers can check this constraint to verify that the computed effective elastic moduli do satisfy the isotropy constraint. It should also be noted here that in traditional AH method, rectangular unit cells are preferred in that they are easier to apply the periodic boundary condition. In the proposed CBNH method, however, any reasonable shape (rectangle, triangle or hexagon) of the unit cells are handled exactly in the same manner. This can be one of the advantages of the proposed CBNH method.

4.4 Kagome lattice

In this example we consider the Kagome-like beam structure as shown in Fig. 11. Traditional AH method cannot be directly applied to calculate the effective elastic moduli of beam-like or truss-like PUCs since their $\boldsymbol{B}$ matrices are not consistent with the $\boldsymbol{D}$ matrix of continuum, making the evaluation of (17) and (18) not possible. In detail, the stiffness matrices of beam or truss elements are calculated in *local* coordinate system, but the assembly of pseudo nodal loads (17) and effective elastic moduli (18) relies on the $\boldsymbol{B}$ and $\boldsymbol{D}$ in *global* coordinate system. For example, in the planar linear truss element, $\boldsymbol{B}$ is of dimension 1×2 while $\boldsymbol{D}$ is of dimension 3×3, making it impossible to calculate $\boldsymbol{B}^{\mathrm{T}}\boldsymbol{D}$. Sigmund (1994a, 1994b) proposes to regard the truss element as a special continuum element with two nodes so that an equivalent $\boldsymbol{B}$ matrix of dimension 3×4 can be defined. But this trick is not general in the sense that it is not easy to find the corresponding formulation for beam, plate and shell elements.

In our CBNH method, however, there is no difficulties in dealing with the Kagome-like beam structures as shown in Fig. 11, the working procedure is exactly the same as that of continua structures. Refer to Fig. 11, let L denote the edge length, then the primitive translational vectors are

$$\boldsymbol{a}^{(1)} = L\begin{bmatrix} 1 \\ \sqrt{3} \end{bmatrix}, \quad \boldsymbol{a}^{(2)} = L\begin{bmatrix} -1 \\ \sqrt{3} \end{bmatrix}. \tag{60}$$

Note that in this example there are only four boundary nodes A, E, C and D. Among these nodes only A and E are independent, the displacement of the other nodes can be expressed using nodes A and E with the affine boundary condition,

$$\begin{aligned} \boldsymbol{u}_{\mathrm{C}} &= \boldsymbol{u}_{\mathrm{A}} + \bar{\boldsymbol{\varepsilon}}\boldsymbol{a}^{(1)}, \\ \boldsymbol{u}_{\mathrm{D}} &= \boldsymbol{u}_{\mathrm{E}} + \bar{\boldsymbol{\varepsilon}}\boldsymbol{a}^{(2)}. \end{aligned} \tag{61}$$

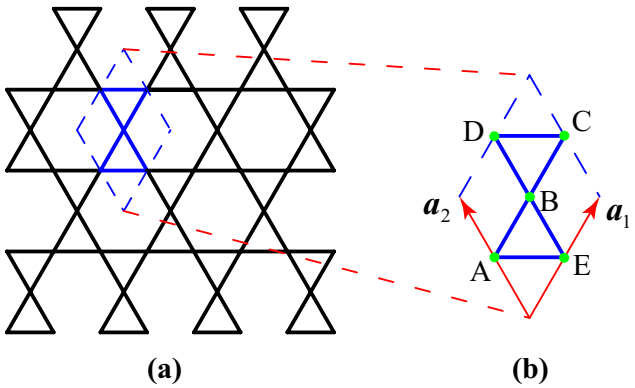

Fig. 11 Kagome structure. **a** Periodic tessellation of unit cells, and **b** one unit cell

Table 4 Effective elastic moduli of the Kagome-like beam structure

	$D^{\heartsuit}_{11}$	$D^{\heartsuit}_{22}$	$D^{\heartsuit}_{66}$	$D^{\heartsuit}_{26}$	$D^{\heartsuit}_{16}$	$D^{\heartsuit}_{12}$
CBNH	14.2848	14.2848	4.7621	0	0	4.7601
Equation (62)	14.2844	14.2844	4.7619	0	0	4.7605

The effective elastic moduli of the Kagome-like beam structure has analytical results (Vigliotti and Pasini 2012a) as follows,

$$\boldsymbol{D}^{\heartsuit} = \frac{\sqrt{3}E_s}{8L^3} \times \begin{bmatrix} 3\left(AL^2+2I_{zz}\right) & AL^2-6I_{zz} & 0 \\ AL^2-6I_{zz} & 3\left(AL^2+2I_{zz}\right) & 0 \\ 0 & 0 & AL^2+6I_{zz} \end{bmatrix}, \tag{62}$$

where E_s is the Young's modulus of base material, A and I_{zz} are the cross-sectional area and the polar moment of inertia, respectively. For circular cross-section bars, let r be the radius, the cross-sectional area and polar moment of inertia can be given by

$$A = \pi r^2, \quad I_{zz} = \frac{1}{2}\pi r^4. \tag{63}$$

It can be verified that Eq. (62) also satisfies the isotropy constraint (59), thus the Kagome structure also belongs the isotropic material in macroscopic scale.

In Table 4 we compare the effective elastic moduli calculated by CBNH and Eq. (62). As can be found from Table 4, our results agree very well with the analytical ones, demonstrating the effectiveness of the proposed CBNH method to deal with PUCs comprising of discrete structural elements.

4.5 Three-dimensional example: unidirectional boron/aluminum laminate

As shown in Fig. 12, in this example we calculate the effective moduli of the unidirectional laminate composed of the aluminum matrix (yellow region) and boron fiber (green region). Material properties of the aluminum matrix are: $E = 6.83 \times 10^4$ MPa, $\nu = 0.3$. Material properties of the boron fiber are: 3.793×10^5 MPa, $\nu = 0.1$. The unit cell is of dimension $1 \times 1 \times 1$. The radius of the fiber is 0.3868, making the volume fraction of the fiber inclusion to be 47%. The affine boundary conditions of the box-like unit cell are similar to that of the square unit cells as illustrated abovementioned, but now node pairs of corner nodes, edge nodes, and face nodes need to be taken into account. Let L denote the edge length, the primitive translational vectors are

$$\boldsymbol{a}^{(1)} = L\begin{bmatrix}1\\0\\0\end{bmatrix}, \quad \boldsymbol{a}^{(2)} = L\begin{bmatrix}0\\1\\0\end{bmatrix}, \quad \boldsymbol{a}^{(3)} = L\begin{bmatrix}0\\0\\1\end{bmatrix}. \tag{64}$$

Select the corner node D, the edge nodes (DA), (DC), (DH), and the surface nodes (ABCD), (ADHE), (DCGH) as the independent nodes, then the affine boundary conditions can be given by the following sets of equations.

$$\begin{cases} \boldsymbol{u}_{(\mathrm{AB})} = \boldsymbol{u}_{(\mathrm{CD})} + \boldsymbol{\varepsilon}\boldsymbol{a}_1, \\ \boldsymbol{u}_{(\mathrm{GH})} = \boldsymbol{u}_{(\mathrm{CD})} + \boldsymbol{\varepsilon}\boldsymbol{a}_3, \\ \boldsymbol{u}_{(\mathrm{EF})} = \boldsymbol{u}_{(\mathrm{CD})} + \boldsymbol{\varepsilon}(\boldsymbol{a}_1 + \boldsymbol{a}_3), \end{cases} \tag{65}$$

$$\begin{cases} \boldsymbol{u}_{(\mathrm{BC})} = \boldsymbol{u}_{(\mathrm{AD})} + \boldsymbol{\varepsilon}\boldsymbol{a}_2, \\ \boldsymbol{u}_{(\mathrm{EH})} = \boldsymbol{u}_{(\mathrm{AD})} + \boldsymbol{\varepsilon}\boldsymbol{a}_3, \\ \boldsymbol{u}_{(\mathrm{FG})} = \boldsymbol{u}_{(\mathrm{AD})} + \boldsymbol{\varepsilon}(\boldsymbol{a}_2 + \boldsymbol{a}_3), \end{cases} \tag{66}$$

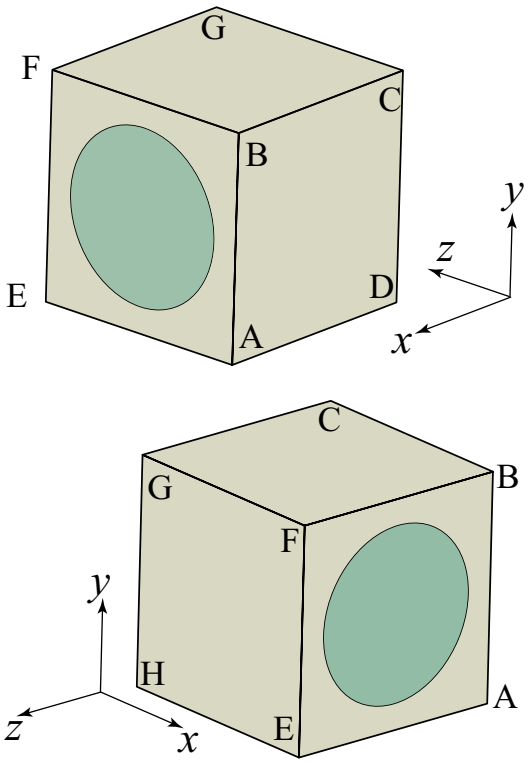

Fig. 12 Unit cell of unidirectional composite

Table 5 Engineering elastic constants of unidirectional boron/aluminum laminate

Elastic constants	CBNH	Xia (Xia et al. 2003)	Sun (Sun and Vaidya 1996)	Chamis (Chamis et al. 1983)	Test data (Kenaga et al. 1987)
E_1 (GPa)	215	214	215	214	216
E_2 (GPa)	144	143	144	156	140
G_{12} (GPa)	54.3	54.2	57.2	62.6	52
G_{23} (GPa)	45.8	45.7	45.9	43.6	–
ν_{12}	0.195	0.195	0.19	0.20	0.29
ν_{23}	0.255	0.253	0.29	0.31	–

$$\begin{cases} \boldsymbol{u}_{(\mathrm{AE})} = \boldsymbol{u}_{(\mathrm{DH})} + \boldsymbol{\varepsilon a}_1, \\ \boldsymbol{u}_{(\mathrm{CG})} = \boldsymbol{u}_{(\mathrm{DH})} + \boldsymbol{\varepsilon a}_2, \\ \boldsymbol{u}_{(\mathrm{BF})} = \boldsymbol{u}_{(\mathrm{DH})} + \boldsymbol{\varepsilon}(\boldsymbol{a}_1 + \boldsymbol{a}_2), \end{cases} \tag{67}$$

$$\begin{cases} \boldsymbol{u}_{\mathrm{EFGH}} = \boldsymbol{u}_{\mathrm{ABCD}} + \boldsymbol{\varepsilon a}_3, \\ \boldsymbol{u}_{\mathrm{BCGF}} = \boldsymbol{u}_{\mathrm{ADHE}} + \boldsymbol{\varepsilon a}_2, \\ \boldsymbol{u}_{\mathrm{ABFE}} = \boldsymbol{u}_{\mathrm{DCGH}} + \boldsymbol{\varepsilon a}_1, \end{cases} \tag{68}$$

$$\begin{cases} \boldsymbol{u}_{\mathrm{A}} = \boldsymbol{u}_{\mathrm{D}} + \boldsymbol{\varepsilon a}_1, \\ \boldsymbol{u}_{\mathrm{B}} = \boldsymbol{u}_{\mathrm{D}} + \boldsymbol{\varepsilon}(\boldsymbol{a}_1 + \boldsymbol{a}_2), \\ \boldsymbol{u}_{\mathrm{C}} = \boldsymbol{u}_{\mathrm{D}} + \boldsymbol{\varepsilon a}_2, \end{cases} \tag{69}$$

$$\begin{cases} \boldsymbol{u}_{\mathrm{E}} = \boldsymbol{u}_{\mathrm{D}} + \boldsymbol{\varepsilon}(\boldsymbol{a}_1 + \boldsymbol{a}_3), \\ \boldsymbol{u}_{\mathrm{F}} = \boldsymbol{u}_{\mathrm{D}} + \boldsymbol{\varepsilon}(\boldsymbol{a}_1 + \boldsymbol{a}_2 + \boldsymbol{a}_3), \\ \boldsymbol{u}_{\mathrm{G}} = \boldsymbol{u}_{\mathrm{D}} + \boldsymbol{\varepsilon}(\boldsymbol{a}_2 + \boldsymbol{a}_3), \\ \boldsymbol{u}_{\mathrm{H}} = \boldsymbol{u}_{\mathrm{D}} + \boldsymbol{\varepsilon a}_3. \end{cases} \tag{70}$$

Obviously the unit cell as shown in Fig. 12 belongs to the orthotropic continuum, so its effective elasticity matrix can be written as

$$\boldsymbol{D} = \begin{bmatrix} D_{11} & D_{12} & D_{13} & 0 & 0 & 0 \\ D_{12} & D_{22} & D_{23} & 0 & 0 & 0 \\ D_{13} & D_{23} & D_{33} & 0 & 0 & 0 \\ 0 & 0 & 0 & D_{44} & 0 & 0 \\ 0 & 0 & 0 & 0 & D_{55} & 0 \\ 0 & 0 & 0 & 0 & 0 & D_{66} \end{bmatrix}, \tag{71}$$

and its inverse, the compliance matrix is given by

$$\boldsymbol{S} = \begin{bmatrix} S_{11} & S_{12} & S_{13} & 0 & 0 & 0 \\ S_{12} & S_{22} & S_{23} & 0 & 0 & 0 \\ S_{13} & S_{23} & S_{33} & 0 & 0 & 0 \\ 0 & 0 & 0 & S_{44} & 0 & 0 \\ 0 & 0 & 0 & 0 & S_{55} & 0 \\ 0 & 0 & 0 & 0 & 0 & S_{66} \end{bmatrix}. \tag{72}$$

The entries of the compliance matrix are closely related to some engineering constants,

$$\begin{aligned} &S_{11} = \frac{1}{E_1}, \quad S_{22} = \frac{1}{E_2}, \quad S_{33} = \frac{1}{E_3} \\ &S_{12} = -\frac{\nu_{12}}{E_2}, \quad S_{13} = -\frac{\nu_{13}}{E_3}, \quad S_{23} = -\frac{\nu_{23}}{E_3}, \end{aligned} \tag{73}$$

where E_i, G_{ij}, ν_{ij} are engineering constants of the orthotropic continuum that can be tested experimentally.

Final calculated effective elastic moduli are given by

$$\begin{aligned} &D^{\heartsuit}_{11} = 230.6434, \quad D^{\heartsuit}_{22} = 160.8435, \\ &D^{\heartsuit}_{33} = 160.8197, \quad D^{\heartsuit}_{23} = 46.2532, \\ &D^{\heartsuit}_{13} = 40.3384, \quad D^{\heartsuit}_{12} = 40.3387, \\ &D^{\heartsuit}_{44} = 45.7929, \quad D^{\heartsuit}_{55} = 54.2883, \\ &D^{\heartsuit}_{66} = 54.3029. \end{aligned} \tag{74}$$

This example has been tested for several times in the literature, where the results are expressed as the engineering constants. In addition, experimental data are also available (Kenaga et al. 1987), making it possible to verify the applicability of the numerical homogenization methods to practical engineering composite materials. In Table 5 we compare the engineering elastic constants obtained by the proposed CBNH method and the ones in the literature. From this table it can be found that our results agree pretty well with the other numerical methods and the experiment results, demonstrating the effectiveness of the proposed method.

4.6 Cubic + octet foam: the stiffest isotropic microstructure

Recently, it is showed that (Berger et al. 2017) the cubic + octet foam (as shown in Fig. 13) is one of the stiffest isotropic microstructure in the sense that its Young's modulus, shear modulus and bulk modulus converge to the Hashin–Shtrikman upper bounds in the low relative density limit. Here we verify this fact by the proposed CBNH

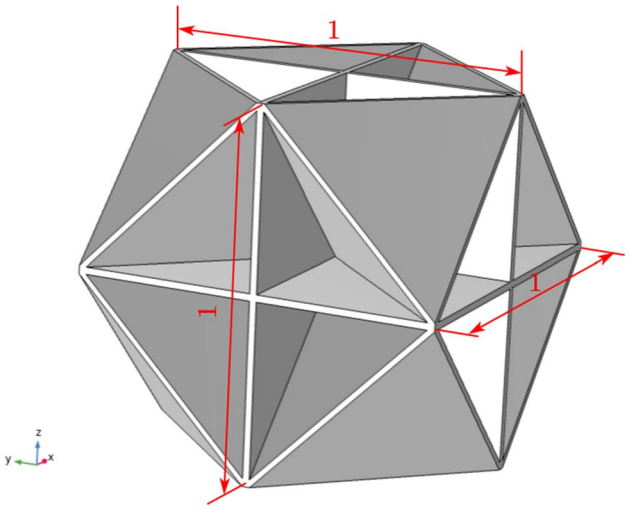

Fig. 13 Cubic + octet foam

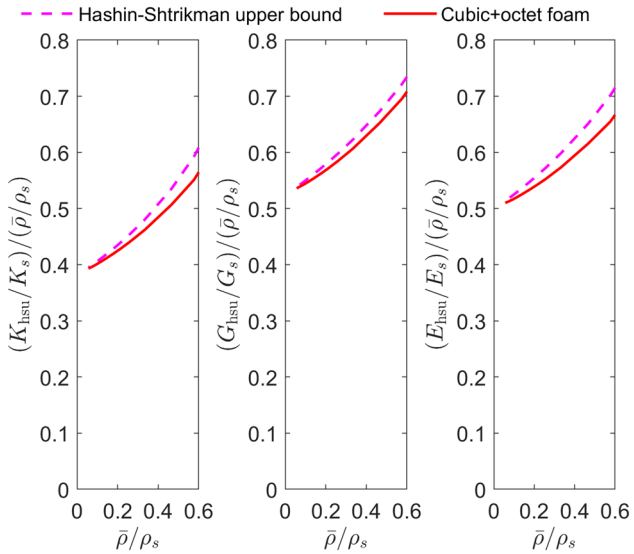

Fig. 14 Bulk, shear and Young's moduli

method. For simplicity we assume that the edge length is 1, then primitive translational vectors can be given by

$$\boldsymbol{a}^{(1)} = \begin{bmatrix} 1 \\ 0 \\ 0 \end{bmatrix}, \quad \boldsymbol{a}^{(2)} = \begin{bmatrix} 0 \\ 1 \\ 0 \end{bmatrix}, \quad \boldsymbol{a}^{(3)} = \begin{bmatrix} 0 \\ 0 \\ 1 \end{bmatrix}. \tag{75}$$

The periodic boundary conditions are exactly the same as that shown in (65) to (70), so will be omitted. The Hashin–Shtrikman upper bounds for single phase microstructure are given by (Berger et al. 2017)

$$\begin{aligned} \frac{K_{\mathrm{hsu}}}{K_{\mathrm{s}}} &= \frac{4G_{\mathrm{s}}\left(\overline{\rho}/\rho_{\mathrm{s}}\right)}{4G_{\mathrm{s}} + 3K_{\mathrm{s}}\left(1-\overline{\rho}/\rho_{\mathrm{s}}\right)}, \\ \frac{G_{\mathrm{hsu}}}{G_{\mathrm{s}}} &= \frac{\left(9K_{\mathrm{s}} + 8G_{\mathrm{s}}\right)\left(\overline{\rho}/\rho_{\mathrm{s}}\right)}{20G_{\mathrm{s}} + 15K_{\mathrm{s}} - 6\left(K_{\mathrm{s}} + 2G_{\mathrm{s}}\right)\left(\overline{\rho}/\rho_{\mathrm{s}}\right)}, \\ E_{\mathrm{hsu}} &= \frac{9G_{\mathrm{hsu}}K_{\mathrm{hsu}}}{3K_{\mathrm{hsu}} + G_{\mathrm{hsu}}}, \end{aligned} \tag{76}$$

where K_{hsu}, G_{hsu} and E_{hsu} denote the Hashin–Shtrikman upper bounds of bulk modulus, shear modulus, and Young's modulus, respectively, K_{s}, G_{s}, E_{s} and ρ_{s} denote the bulk modulus, shear modulus, Young's modulus, and density of constituent solid material, respectively, $\overline{\rho}$ denotes the average density of the microstructure; $\overline{\rho}/\rho_{\mathrm{s}}$ denote the volume fraction of the microstructure, which can be tuned by varying the thickness of each plate.

According to Berger et al. (2017), the thickness of the octet plates and the cubic plates are not the same, we construct the microstructure using $t_{\mathrm{c}}/t_{\mathrm{o}} = 8\sqrt{3}/9$, here t_{c} is the thickness of the walls forming the cubic foam while t_{o} is the thickness of the walls forming the octet foam.

In order to appropriately deal with the joints of the web members we use second-order tetrahedron elements to discretion the microstructure. In Fig. 14 we show the computed bulk, shear and Young's moduli of the cubic + octet foam. The Hashin–Shtrikman upper bounds of these moduli for an isotropic continuum are also shown for purpose of comparison. All the moduli are given in a dimensionless fashion so that the results are independent of the material properties of the constituent solid material. As shown in Fig. 14, the combined cubic + octet foam performs very well in the low-density limit and the computed bulk, shear and Young's moduli coincide with that of the Hashin–Shtrikman upper bounds.

5 Numerical examples for inverse homogenization problems

In this section we test the applicability of the proposed CBNH method to the inverse design problems of microstructures. Both discrete and continuum microstructures are considered. As mentioned in Sect. 3.4, the stopping criteria of the inverse design process are in two folds, i.e., the rule of maximum iterations and the KKT condition. Take the MATLAB function *fmincon* as an example, the rule of maximum iterations can be controlled by setting the option "MaxIterations" to a user-defined positive integer, the KKT tolerance can be controlled by setting the option "OptimalityTolerance" to a user-defined small positive real number. Throughout this section, we set "MaxIterations" to 1000, and "OptimalityTolerance" to 1×10^{-6}.

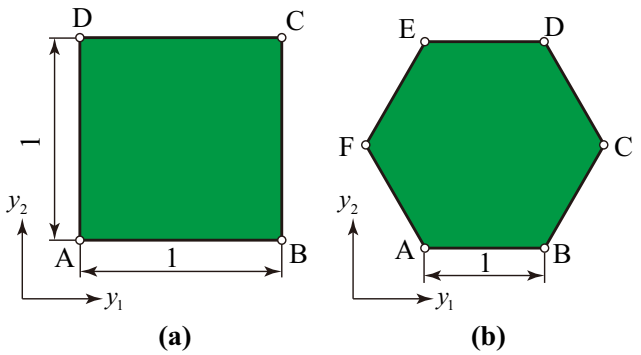

Fig. 15 Design domain of the inverse homogenization problems. **a** Square base cell. **b** Hexagonal base cell

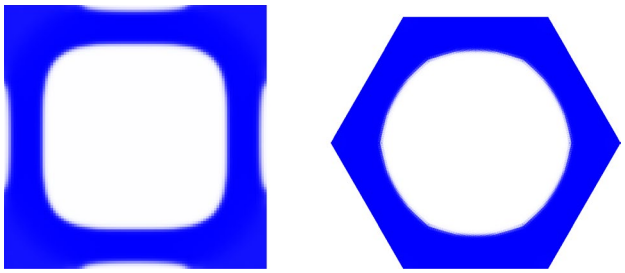

(a) square base cell **(b)** hexagonal base cell

Fig. 16 Final optimized microstructure with maximum bulk modulus. The objective function value $\kappa^{\heartsuit}$ is 167.1147 for the square base cell, and 177.5923 for the hexagonal base cell

5.1 Design of microstructure with maximum bulk modulus

In this example we attempt to find the microstructure that exhibits maximum bulk modulus, here the bulk modulus is defined as the mean value of D_{11}, D_{12}, D_{21}, and D_{22}. The microstructure is composed of two phases, the first one is an isotropic material with $E = 1000$, $\nu = 0.3$; the second one is void. Prescribed material volume fraction is $\gamma = 0.5$. The mathematical model can be given by

$$\begin{aligned} &\text{find} && \boldsymbol{\xi} = [\xi_1, \xi_2, \ldots, \xi_n]^{\top}, \\ &\text{maximize} && \kappa^{\heartsuit} = \tfrac{1}{4}\left(D_{11}^{\heartsuit} + D_{12}^{\heartsuit} + D_{21}^{\heartsuit} + D_{22}^{\heartsuit}\right), \\ &\text{subject to} && \sum_{i=1}^{n_{\text{nele}}} \xi_i V_i \le \gamma \sum_{i=1}^{n_{\text{nele}}} V_i, \end{aligned} \tag{77}$$

where V_i is the volume of ith element, the continuous design variable $\xi_i \in [0, 1]$ is the elemental fictitious density of ith element.

Two kinds of base cells are considered, one is of square shape (see Fig. 15a) and the other is of hexagonal shape (see Fig. 15b). The affine boundary conditions for these two base cells are the same with that presented in Sects. 4.1 and 4.3, respectively. The whole work flow of the inverse homogenization process is shown in Fig. 4. For this specific example, the sensitivity of the objective function is given by

$$\frac{\partial \kappa^{\heartsuit}}{\partial \xi_i} = \frac{1}{4}\left(\frac{\partial D_{11}^{\heartsuit}}{\partial \xi_i} + \frac{\partial D_{12}^{\heartsuit}}{\partial \xi_i} + \frac{\partial D_{21}^{\heartsuit}}{\partial \xi_i} + \frac{\partial D_{22}^{\heartsuit}}{\partial \xi_i}\right). \tag{78}$$

In this paper we use the density-based method to do the topology optimization, i.e., the Young's modulus of ith element is interpolated using the ith design variable as

$$E_i = \xi_i^3 E_0 + \left(1 - \xi_i^3\right) E_{\min}, \tag{79}$$

where $\xi_i \in [0, 1]$ is the design variable, E_0 is the Young's modulus of the ith element when it is filled with solid

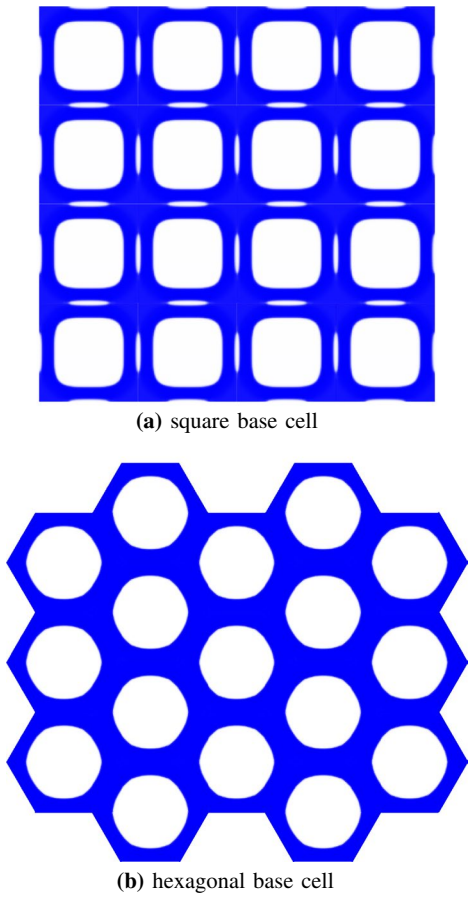

(a) square base cell **(b)** hexagonal base cell

Fig. 17 Periodic tessellation of unit cells

material while $E_{\min}$ is the Young's modulus of the element when it is void. We set $E_{\min} = 1 \times 10^{-6} E_0$. By the way, we mention that the design variable should undergo the commonly used filter process and projection process before it can be used to interpolate the elemental stiffness matrix, the details can be found in our past work (Zhou et al. 2018a, b, 2019, 2021) and will be omitted here.

Final optimized microstructure is shown in Fig. 16, the corresponding effective elastic moduli and bulk modulus of the square base cell is

$$\begin{aligned} \boldsymbol{D}^{\heartsuit}_{\text{sq}} &= \begin{bmatrix} 290.9945 & 43.2350 & 0.0006 \\ 43.2350 & 290.9945 & -0.0006 \\ 0.0006 & -0.0006 & 12.9736 \end{bmatrix}, \\ \kappa^{\heartsuit} &= 167.1147; \end{aligned} \tag{80}$$

and that of the hexagonal base cell is

$$\begin{aligned} \boldsymbol{D}^{\heartsuit}_{\text{hex}} &= \begin{bmatrix} 246.3857 & 108.6639 & -0.0002 \\ 108.6639 & 246.3617 & -0.0001 \\ -0.0002 & -0.0001 & 68.8632 \end{bmatrix}, \\ \kappa^{\heartsuit} &= 177.5923. \end{aligned} \tag{81}$$

By checking the isotropy constraint (59) on the expressions of the effective elastic moduli (80) and (81), one can find that the optimized square microstructure belongs to the (macroscopically) orthotropic continuum while the optimized hexagonal microstructure belongs to the isotropic material. The bulk modulus of the hexagonal microstructure (177.5923, Fig. 16a) is a little larger than that of the square microstructure (167.1147, Fig. 16b). Assuming that the weak phase is purely void, the famous Hashin–Shtrikman bounds of the bulk modulus can be explicitly calculated as (Sigmund 2000)

$$\begin{aligned} \kappa_{\text{l}}^{\text{HS}} &= 0, \\ \kappa_{\text{u}}^{\text{HS}} &= \frac{\gamma \kappa \mu}{(1-\gamma)\kappa + \mu} = 185.1852, \end{aligned} \tag{82}$$

where $\kappa = \frac{E}{2(1-\nu)} = 714.2857$, $\mu = \frac{E}{2(1+\nu)} = 384.6154$ are the bulk modulus and shear modulus of the base material, respectively, $\kappa_{\text{l}}^{\text{HS}}$ and $\kappa_{\text{u}}^{\text{HS}}$ are the lower and upper bounds, respectively. From (82) it can be found that the microstructures we design do get close to the theoretical upper bound of the bulk modulus. $\kappa^{\heartsuit}/\kappa_{\text{u}}^{\text{HS}}$ is 90.24% for the square cell while 95.90% for the hexagonal cell, thus demonstrating the effectiveness of the proposed inverse homogenization procedure. In Fig. 17 we show the periodic materials composed of the base cells in Fig. 16.

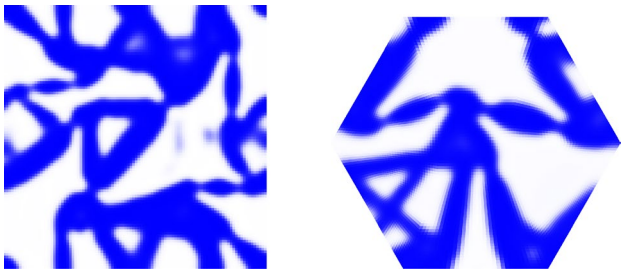

(a) square base cell **(b)** hexagonal base cell

Fig. 18 Final optimized microstructure with negative Poisson's ratio. The objective function value $\nu^{\heartsuit}$ is −0.8587 for the square base cell, and −0.8583 for the hexagonal base cell

5.2 Design of microstructure with negative Poisson's ratio

In this example we attempt to find the layout of *isotropic* microstructures having negative Poisson's ratio, which is defined as $\nu^{\heartsuit} = D^{\heartsuit}_{12}/D^{\heartsuit}_{11}$. Properties of the constituent materials are the same as that in Sect. 5.1. Construction of materials exhibiting negative Poisson's ratio using continuum constituent materials is known to be difficult (Sigmund 1994b; Xia and Breitkopf 2015; Andreassen et al. 2014). In order to make the design process successful, some additional constraints should be applied to render the problem well-posed. The mathematical model used in this paper is given as

$$\begin{aligned} &\text{find} && \boldsymbol{\xi} = [\xi_1, \xi_2, \ldots, \xi_n]^{\top}, \\ &\text{minimize} && \nu^{\heartsuit} = D^{\heartsuit}_{12}/D^{\heartsuit}_{11}, \\ &\text{subject to} && \begin{cases} \sum_{i=1}^{n_{\text{nele}}} \xi_i V_i \le \gamma \sum_{i=1}^{n_{\text{nele}}} V_i, \\ D^{\heartsuit}_{11} + D^{\heartsuit}_{12} + D^{\heartsuit}_{21} + D^{\heartsuit}_{22} \ge 0.01E, \\ \dfrac{\sum_{i,j=1}^{3} \left(D^{\text{iso}}_{ij} - D^{\heartsuit}_{ij} \right)^2}{\left(D^{\text{iso}}_{11} \right)^2} \le 1 \times 10^{-5}. \end{cases} \end{aligned} \tag{83}$$

The constraints used in (83) warrants some explanations. The first constraint restricts the material usage of the solid material. The second constraint requires that the bulk modulus of the optimized microstructure cannot be lower than a prescribed value so that the unwanted node hinges would not be presented in the final optimized design. The third constraint implies that the isotropic microstructure is preferred, D^{iso}_{ij} denotes the elastic tensor of the corresponding isotropic continuum and its components are defined as

$$\begin{aligned} D^{\text{iso}}_{11} &= D^{\text{iso}}_{22} = \frac{1}{2}\left(D^{\heartsuit}_{11} + D^{\heartsuit}_{22} \right), \\ D^{\text{iso}}_{12} &= D^{\text{iso}}_{21} = D^{\heartsuit}_{12}, \\ D^{\text{iso}}_{66} &= \frac{D^{\text{iso}}_{11} - D^{\text{iso}}_{12}}{2}, \\ D^{\text{iso}}_{16} &= D^{\text{iso}}_{26} = 0. \end{aligned} \tag{84}$$

(a) square base cell

(b) hexagonal base cell

Fig. 19 Periodic tessellation of unit cells

(a) Final optimized microstructure.

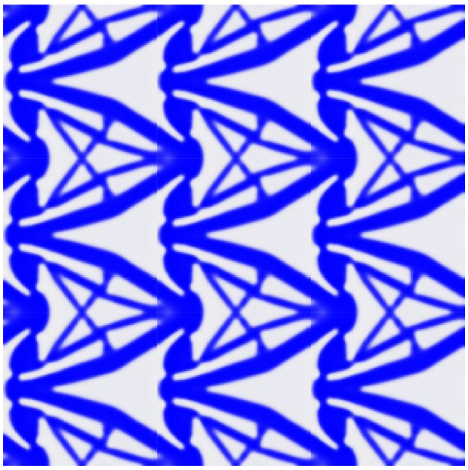

(b) Periodic tessellation of unit cells.

Fig. 20 Final optimized microstructure with negative Poisson's ratio considering symmetry pre-assumptions. The objective function value is $\nu^{\heartsuit} = -0.8587$

As in Sect. 5.1, both the square and hexagonal cells are considered as the design domain. Final optimized microstructures are shown in Fig. 18 while the periodic tessellation of these microstructures are shown in Fig. 19. The corresponding effective elastic moduli and Poisson's ratio of the square base cell is

$$\begin{aligned} \boldsymbol{D}^{\heartsuit}_{\text{sq}} &= \begin{bmatrix} 34.8389 & -29.9156 & 0.0028 \\ -29.9156 & 34.9923 & 0.0075 \\ 0.0028 & 0.0075 & 32.3959 \end{bmatrix}, \\ \nu^{\heartsuit}_{\text{sq}} &= -0.8587, \end{aligned} \tag{85}$$

and the hexagonal base cell is

$$\begin{aligned} \boldsymbol{D}^{\heartsuit}_{\text{hex}} &= \begin{bmatrix} 34.7372 & -29.8144 & 0.0003 \\ -29.8144 & 34.8919 & 0.0013 \\ 0.0003 & 0.0013 & 32.3031 \end{bmatrix}, \\ \nu^{\heartsuit}_{\text{hex}} &= -0.8583. \end{aligned} \tag{86}$$

Due to stability constraint, the Poisson's ratio of an isotropic material should be in the range $[-1, 1]$ in plane stress case. Thus the microstructures we design in this example do get close to the lower bound. Since no symmetry pre-assumptions are made when solving (83), the microstructures shown in Fig. 18 do not exhibit obvious symmetry, though the isotropy constraint [see the third constraint in (83)] is applied. In order to find optimized microstructure satisfying symmetry property, we manually requires that the design variables corresponding to the symmetric elements in the upper half and lower half have exactly the same values, this way the microstructure as shown in Fig. 20 is obtained. As remarked by Milton and Cherkaev (1995), the microstructure with negative Poisson's ratio can unfold in some senses when subject to stretching loads. In Figs. 19 and 20 one can find many joint-like delicate connections which contributes to the unfolding behavior under stretching loads. The microstructure in Fig. 20 looks similar to the ones in the literature (Milton and Cherkaev 1995; Andreassen et al. 2014; Sigmund 2000) but has more slim bars.

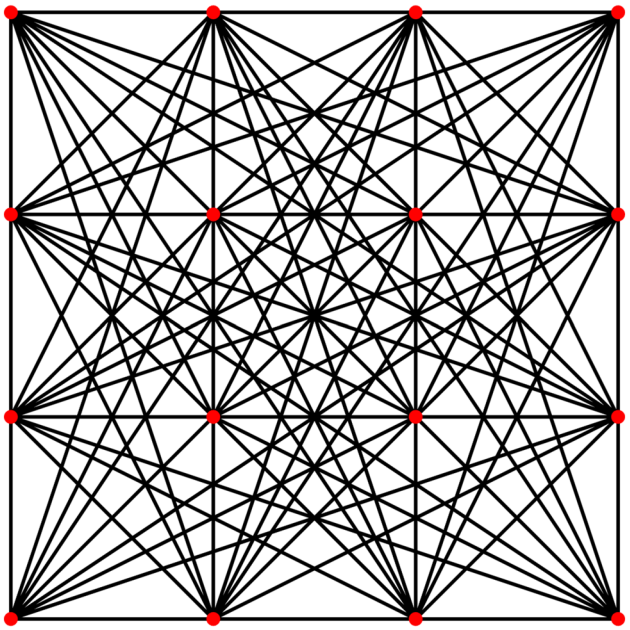

Fig. 21 The ground structure of the microstructure

5.3 Design of truss-like isotropic material with unitary Poisson's ratio

As mentioned in the previous example, the Poisson's ratio of an *isotropic* material should be in the range $[-1, 1]$ in plane stress case. In this example we attempt to find the truss-like microstructure with Poisson's ratio to be 1.

In plane stress case, the Poisson's ratio of isotropic continuum is defined as

$$\nu = \frac{D_{12}}{D_{11}} = \frac{D_{11} - 2D_{66}}{D_{11}} = 1 - \frac{2D_{66}}{D_{11}}. \tag{87}$$

Thus the microstructure with unitary Poisson's ratio is equivalent to the one with zero shear modulus (i.e., $D_{66} = 0$). The mathematical model for this problem can therefore can written as

$$\begin{aligned} &\text{find} && \boldsymbol{\xi} = [\xi_1, \xi_2, \dots, \xi_n]^\top \\ &\text{maximize} && \kappa^\heartsuit \\ &\text{subject to} && \begin{cases} D_{11} \geq 0.01E \\ D_{22} \geq 0.01E \\ D_{12} \geq 0.01E \\ D_{66} = 0 \\ \sum_{i,j} \dfrac{\left(D_{ij}^\heartsuit - D_{ij}^{\text{iso}}\right)^2}{\left(D_{11}^{\text{iso}}\right)^2} \leq 1 \times 10^{-5} \\ \sum_{i=1}^{n} \xi_i \leq 8, \end{cases} \end{aligned} \tag{88}$$

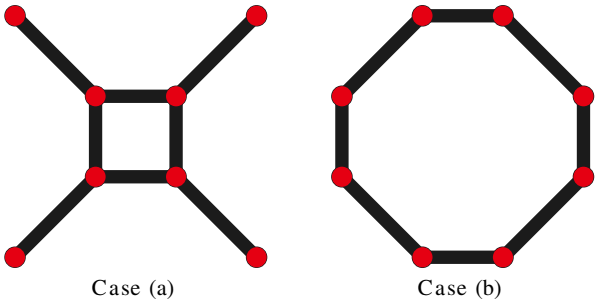

Fig. 22 Two possible final optimized microstructure with unitary Poisson's ratio. The objective function value $\kappa^\heartsuit = 0.2612$ for both cases

where the continuous design variable $\xi_i \in [0, 1]$ denotes the topological variable of ith bar and reveals the existence of this bar, the first three constraints restrict the lower bounds of D_{11}, D_{22}, and D_{12}, respectively, the fourth constraint requires the shear modulus to be zero, the fifth constraint demands that the designed microstructure should belong to the macroscopically isotropic continuum, D_{ij}^{iso} has been defined in (84), the last constraint sets the upper limit of material usage.

The topology optimization of truss-like microstructures can still rely on the idea of the density method, i.e., the interpolation scheme (79) can still be used here. The design domain is a ground structure as shown in Fig. 21. If $\xi_i = 0$ then ith element would disappear in the final optimized design; if $\xi_i = 1$ then ith element would be retained in the final optimized design. There are in total 16 nodes in Fig. 21, so there will be $\binom{16}{2} = 120$ design variables. Apparently some bars would partially be coincident, and some bars would come across with each other. In order to get rid of the coincidence and crossing of the bars, a special penalty term $r\boldsymbol{\xi}^\top \boldsymbol{P}\boldsymbol{\xi}$ is added to the objective function. Here $\boldsymbol{P} \in \{0, 1\}^{120\times 120}$ is a logical matrix, $P_{ij} = 1$ if ith bar and jth bar are partially coincident or intersecting with each other, otherwise $P_{ij} = 0$; r is a parameter to control the strength of the penalty term.

Two possible final optimized microstructures are shown in Fig. 22 and the periodic tessellation of these microstructures are shown in Fig. 23. Note that in Case (b) of Fig. 23, the vertical and horizontal bars are twice as thick as the inclined bars since they are on the borders of the unit cell. Interestingly, the effective elasticity tensor of the two microstructures in Fig. 22 are exactly the same,

$$\boldsymbol{D}^\heartsuit = 0.2612 \begin{bmatrix} 1 & 1 & 0 \\ 1 & 1 & 0 \\ 0 & 0 & 0 \end{bmatrix}. \tag{89}$$

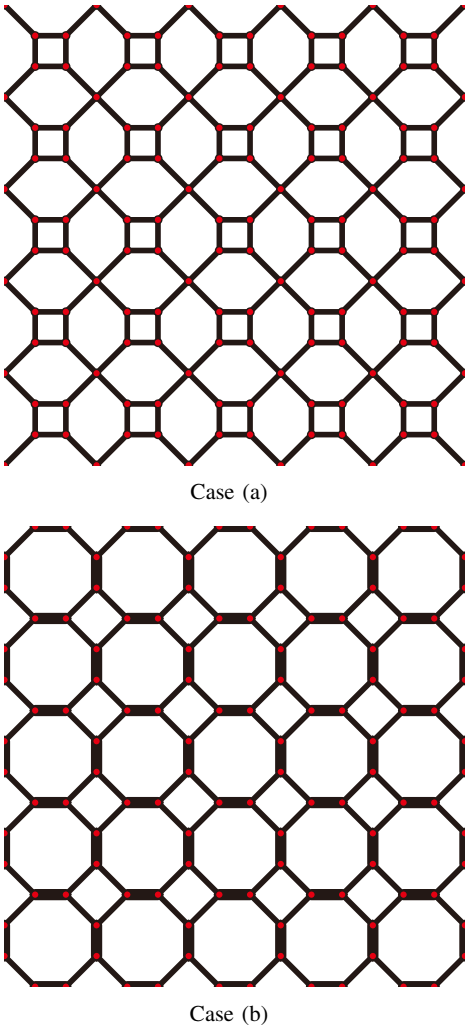

Fig. 23 Periodic tessellation of the unit cells in Fig. 22

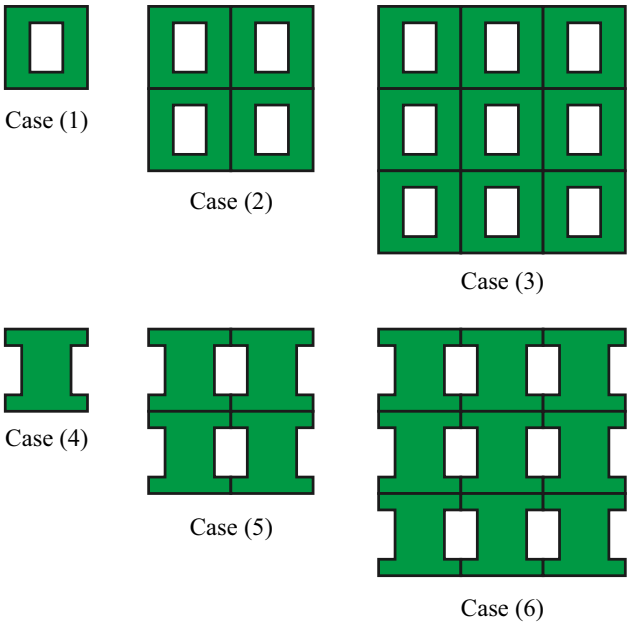

Fig. 24 Unit cells of different shapes and sizes

In two-dimensional case, unitary Poisson's ratio means that under longitude compression loads, the lateral expansion displacement is equal to the longitude compression displacement for a square shape material. Investigating the periodic tessellations as shown in Fig. 23, one can find that both materials are composed of square and hexagonal microstructures with exactly equal edge lengths, which is consistent with the unitary Poisson's ratio.

We mention here that since the number of design variables is not large, and the evaluation of the objection function and constraint is not time-consuming, it is also possible to use non-gradient algorithm, e.g., Khatir et al. (2019, 2020) and Khatir and Abdel Wahab (2019), to solve this example. But throughout this section, we use gradient-based interior-point algorithm to solve the optimization problems.

6 Discussion

6.1 Scale-invariance of the Cauchy–Born rule based numerical homogenization method

In this section we verify the scale-invariance of the proposed CBNH method. A well-established numerical homogenization method should hold the property of scale-invariance, i.e., the computed effective elastic moduli must be the same for all possible choice of basic unit cells. In this example we test the scale-invariance of the proposed CBNH method by computing the effective elastic moduli of all the six kinds of unit cells as shown in Fig. 24. In Table 6 we list the computed effective elastic moduli of all the six unit cells, it can be found from this table that the proposed CBNH method does hold the scale-invariance property. Meanwhile, the RVE method is also tested on these six unit cells, the results are listed in Table 7, from which the scale dependency of the RVE method can be clearly seen. When more unit cells are included in the RVE method, the computed elastic moduli gradually converge to the ones by the proposed CBNH method from above.

Table 6 Scale-invariance of the CBNH method

	$D_{11}^{\heartsuit}$	$D_{22}^{\heartsuit}$	$D_{66}^{\heartsuit}$	$D_{26}^{\heartsuit}$	$D_{16}^{\heartsuit}$	$D_{12}^{\heartsuit}$
Case (1)	12.858	17.435	2.663	0	0	3.149
Case (2)	12.858	17.435	2.663	0	0	3.149
Case (3)	12.858	17.435	2.663	0	0	3.149
Case (4)	12.858	17.435	2.663	0	0	3.149
Case (5)	12.858	17.435	2.663	0	0	3.149
Case (6)	12.858	17.435	2.663	0	0	3.149

Table 7 Scale-dependency of the RVE method

	$D_{11}^{\heartsuit}$	$D_{22}^{\heartsuit}$	$D_{66}^{\heartsuit}$	$D_{26}^{\heartsuit}$	$D_{16}^{\heartsuit}$	$D_{12}^{\heartsuit}$
Case (1)	13.161	17.708	4.620	0	0	3.306
Case (2)	13.001	17.567	3.628	0	0	3.217
Case (3)	12.951	17.522	3.283	0	0	3.192
Case (4)	13.001	18.948	4.787	0	0	3.611
Case (5)	12.933	18.231	3.908	0	0	3.393
Case (6)	12.909	17.973	3.510	0	0	3.314

7 Conclusion

In this paper the Cauchy–Born hypothesis based numerical homogenization method is proposed to calculate the effective elastic moduli of PUCs. Due to its simplicity, it can be easily implemented using commercial FEA software. In comparison with the method of representative volume element, which is commonly used in the community of composite mechanics, the proposed method holds the property of scale-invariance, so is much more accurate. In comparison with the asymptotic expansion based homogenization method, which is commonly used in the community of topology optimization, the proposed method can be freely applied to both continuum and discrete (e.g., truss, beam, plate and shell) unit cells without any modification to the FEA codes. In addition, the proposed method can easily handle the unit cells with complex geometries (e.g., hexagonal, Kagome-like, or triangular unit cells) since the affine boundary conditions in the proposed method have naturally considered the primitive translational vectors. Owing to these advantages, the proposed method can definitely be applied to the problems of inverse homogenization, and it turns out that the whole inverse homogenization process, including both the homogenization procedure and the sensitivity analysis procedure, can be implemented using commercial FEA software in an easy manner.

Supplementary Information The online version supplementary material available at https://doi.org/10.1007/s00158-021-03068-x.

Funding The research is supported by National Natural Science Foundation of China (Grant Nos. 11902180, 11772170, 11991033, 11991030, 11972083), China Postdoctoral Science Foundation (Grant Nos. BX20180156, 2019M650650), and Beijing Science and Technology Commission (Grant No. Z191100004819003).

Declarations

Conflict of interest The authors declare that they have no conflict of interest.

Replication of results All the datasets in this study are generated using our homemade codes. The full datasets, as well as the source codes, can be available from the corresponding author with reasonable request. We also offer some sample codes as Supplementary Material, which can be used to solve the example as shown in Sect. 5.1.

References

Aboudi J (1991) Mechanics of composite materials. Elsevier, Tokyo

Andreassen E, Andreasen CS (2014) How to determine composite material properties using numerical homogenization. Comput Mater Sci 83:488–495. https://doi.org/10.1016/j.commatsci.2013.09.006

Andreassen E, Lazarov BS, Sigmund O (2014) Design of manufacturable 3D extremal elastic microstructure. Mech Mater 69(1):1–10. https://doi.org/10.1016/j.mechmat.2013.09.018

Bakhvalov N, Panasenko G (1984) Homogenisation: averaging processes in periodic media. Kluwer Academic Publishers, Dordrecht

Bendsoe MP, Kikuchi N (1988) Generating optimal topologies in structure design using homogenization method. Comput Methods Appl Mech Eng 71(2):197–224

Bensoussan A, Papanicolaou G, Rockafellar RT (1978) Asymptotic analysis for periodic structures. Elsevier Science Ltd., Tokyo

Berger JB, Wadley HNG, McMeeking RM (2017) Mechanical metamaterials at the theoretical limit of isotropic elastic stiffness. Nature 543(7646):533–537. https://doi.org/10.1038/nature21075

Chamis CC, Center LR, Cleveland O (1983) Simplified composite micromechanics equations for hygral, thermal and mechanical properties

Chandraseker K, Mukherjee S, Mukherjee YX (2006) Modifications to the Cauchy–Born rule: applications in the deformation

of single-walled carbon nanotubes. Int J Solids Struct 43(22–23):7128–7144. https://doi.org/10.1016/j.ijsolstr.2006.03.007
Cheng GD, Cai YW, Xu L (2013) Novel implementation of homogenization method to predict effective properties of periodic materials. Acta Mech Sin 29(4):550–556. https://doi.org/10.1007/s10409-013-0043-0
Christoff BG, Brito-Santana H, Talreja R, Tita V (2020) Development of an ABAQUS^{TM} plug-in to evaluate the fourth-order elasticity tensor of a periodic material via homogenization by the asymptotic expansion method. Finite Elem Anal Des. https://doi.org/10.1016/j.finel.2020.103482
Dong G, Tang Y, Zhao YF (2019) A 149 line homogenization code for three-dimensional cellular materials written in MATLAB. J Eng Mater Technol 141:011005
Ericksen JL (2008) On the Cauchy–Born rule. Math Mech Solids 13(3–4):199–220. https://doi.org/10.1177/1081286507086898
Gasparetto VEL, ElSayed MSA (2021) Multiscale optimization of specific elastic properties and microscopic frequency band-gaps of architectured microtruss lattice materials. Int J Mech Sci. https://doi.org/10.1016/j.ijmecsci.2021.106320
Gibson RF (2016) Principles of composite material mechanics. CRC Press, New York
Guedes J, Kikuchi N (1990) Preprocessing and postprocessing for materials based on the homogenization method with adaptive finite element methods. Comput Methods Appl Mech Eng 83(2):143–198. https://doi.org/10.1016/0045-7825(90)90148-F
Hassani B, Hinton E (1998a) A review of homogenization and topology opimization II—analytical and numerical solution of homogenization equations. Comput Struct 69(6):719–738. https://doi.org/10.1016/S0045-7949(98)00132-1
Hassani B, Hinton E (1998b) A review of homogenization and topology optimization I—homogenization theory for media with periodic structure. Comput Struct 69(6):707–717. https://doi.org/10.1016/S0045-7949(98)00131-X
Hassani B, Hinton E (1999) Homogenization and structural topology optimization. Springer, London
Hutchinson RG, Fleck NA (2006) The structural performance of the periodic truss. J Mech Phys Solids 54(4):756–782. https://doi.org/10.1016/j.jmps.2005.10.008
Ibrahimbegovic A, Wilson EL (1991) A modified method of incompatible modes. Commun Appl Numer Methods 7(3):187–194
Kalamkarov AL, Georgiades AV (2004) Asymptotic homogenization models for smart composite plates with rapidly varying th ickness: Part I—theory. Int J Multiscale Comput Eng 2(1):133–148
Kenaga D, Doyle JF, Sun CT (1987) The characterization of boron/aluminum composite in the nonlinear range as an orthotropic elastic–plastic material. J Compos Mater 21(6):516–531. https://doi.org/10.1177/002199838702100603
Khatir S, Abdel Wahab M (2019) Fast simulations for solving fracture mechanics inverse problems using POD-RBF XIGA and Jaya algorithm. Eng Fract Mech 205:285–300. https://doi.org/10.1016/j.engfracmech.2018.09.032
Khatir S, Abdel Wahab M, Boutchicha D, Khatir T (2019) Structural health monitoring using modal strain energy damage indicator coupled with teaching-learning-based optimization algorithm and isogoemetric analysis. J Sound Vib 448:230–246. https://doi.org/10.1016/j.jsv.2019.02.017
Khatir S, Boutchicha D, Le Thanh C, Tran-Ngoc H, Nguyen TN, Abdel-Wahab M (2020) Improved ann technique combined with Jaya algorithm for crack identification in plates using XIGA and experimental analysis. Theor Appl Fract Mech. https://doi.org/10.1016/j.tafmec.2020.102554
Kittel C (2005) Introduction to solid state physics. Wiley, Hoboken
Milton GW, Cherkaev AV (1995) Which elasticity tensors are realizable? J Eng Mater Technol 117:483–493
Nocedal J, Wright SJ (2006) Numerical optimization, 2nd edn. Springer, New York
Sigmund O (1994b) Materials with prescribed constitutive parameters: an inverse homogenization problem. Int J Solids Struct 31(17):2313–2329
Sigmund O (1995) Tailoring materials with prescribed elastic properties. Mech Mater 20(4):351–368. https://doi.org/10.1016/0167-6636(94)00069-7
Sigmund O (2000) A new class of extremal composites. J Mech Phys Solids 48(2):397–428. https://doi.org/10.1016/S0022-5096(99)00034-4
Sigmund O, Torquato S (1996) Composites with extremal thermal expansion coefficients. Appl Phys Lett 69(21):3203–3205. https://doi.org/10.1063/1.117961
Sigmund O (1994a) Design of material structures using topology optimization. PhD Thesis, Technical University of Denmark
Sun CT, Vaidya RS (1996) Prediction of composite properties from a representative volume element. Compos Sci Technol 56(2):171–179. https://doi.org/10.1016/0266-3538(95)00141-7
Vigliotti A, Pasini D (2012a) Linear multiscale analysis and finite element validation of stretching and bending dominated lattice materials. Mech Mater 46:57–68. https://doi.org/10.1016/j.mechmat.2011.11.009
Vigliotti A, Pasini D (2012) Stiffness and strength of tridimensional periodic lattices. Comput Methods Appl Mech Eng 229–232:27–43. https://doi.org/10.1016/j.cma.2012.03.018
Xia L, Breitkopf P (2015) Design of materials using topology optimization and energy-based homogenization approach in MATLAB. Struct Multidisc Optim 52(6):1229–1241. https://doi.org/10.1007/s00158-015-1294-0
Xia Z, Zhang Y, Ellyin F (2003) A unified periodical boundary conditions for representative volume elements of composites and applications. Int J Solids Struct 40(8):1907–1921. https://doi.org/10.1016/S0020-7683(03)00024-6
Yan J, Cheng G, Liu S, Liu L (2006) Comparison of prediction on effective elastic property and shape optimization of truss material with periodic microstructure. Int J Mech Sci 48(4):400–413. https://doi.org/10.1016/j.ijmecsci.2005.11.003
Yuan Z, Fish J (2008) Toward realization of computational homogenization in practice. Int J Numer Methods Eng 73(3):361–380. https://doi.org/10.1002/nme.2074
Zhou P, Du J, Lü Z (2018a) Hybrid optimization of a vibration isolation system considering layout of structure and locations of components. Struct Multidisc Optim 57(1):1–15. https://doi.org/10.1007/s00158-017-1828-8
Zhou P, Du J, Lü Z (2018b) Simultaneous topology optimization of supporting structure and loci of isolators in an active vibration isolation system. Comput Struct 194(1):74–85. https://doi.org/10.1016/j.compstruc.2017.09.006
Zhou P, Ou G, Du J (2019) Topology optimization of continua considering mass and inertia characteristics. Struct Multidisc Optim 60(2):429–442. https://doi.org/10.1007/s00158-019-02322-7
Zhou P, Peng Y, Du J (2021) Topology optimization of bi-material structures with frequency-domain objectives using time-domain simulation and sensitivity analysis. Struct Multidisc Optim 63(2):575–593. https://doi.org/10.1007/s00158-020-02814-x
Zohdi TI, Wriggers P (2008) An introduction to computational micromechanics. Springer, Heidelberg